POLYTECHNIQUE MONTRÉAL
affiliée à l'Université de Montréal

Real-time OCT surveillance of laser therapy through speckle decorrelation

RAPHAËL MALTAIS-TARIANT
Département de génie physique

Mémoire présenté en vue de l'obtention du diplôme de *Maîtrise ès sciences appliquées*
Génie physique

Décembre 2019

© Raphaël Maltais-Tariant, 2019.

POLYTECHNIQUE MONTRÉAL
affiliée à l'Université de Montréal

Ce mémoire intitulé :

Real-time OCT surveillance of laser therapy through speckle decorrelation

présenté par **Raphaël MALTAIS-TARIANT**
en vue de l'obtention du diplôme de *Maîtrise ès sciences appliquées*
a été dûment accepté par le jury d'examen constitué de :

Frédéric LEBLOND, président
Caroline BOUDOUX, membre et directrice de recherche
Néstor URIBE-PATARROYO, membre et codirecteur de recherche
Michel MEUNIER, membre

DEDICATION

To my family and friends for their support.

À ma famille et mes amis pour leur soutien.

ACKNOWLEDGEMENTS

This work would have not been possible without the outside support I received. I would first like to thank my advisors Prof. Caroline Boudoux and Dr. Néstor Uribe-Patarroyo. They have guided and advised me from the start to the end of this project. I would also like to thank Caroline for all the conference opportunities that allowed me to expand my knowledge of the world of research.

I would also like to thank my lab coworkers for their occasional help: Martin Poinsinet De Sivry-Houle, Xavier Attendu, Simon Brais-Brunet and Édith Ducharme. Martin, Xavier and Simon have always been available to give a second opinion on most of my interrogations. Édith has also participated to the project by making our first experimental set-up as an intern.

I thank the Alazar Tech support team, Romain Deterre and Alexandre Castonguay, for their help making work my first OCT reconstruction program. Their help allowed me to understand how to interact through Labview with the different OCT components.

I would also like to thank Irene Londoño of CHU Ste-Justine Research Center for her help developing and doing the histology analysis of my samples.

Finally, as a broad general thank you, I would like to thank anyone and everyone who takes the time to answer forum questions about programming. It is impossible to know everything in programming and it is only through the knowledge exchanged on forums that we are able to progress.

RÉSUMÉ

La thérapie laser est une technique exploitant les interactions entre la lumière et les tissues biologiques pour traiter des maladies. Par exemple, il est possible d'utiliser l'énergie des photons pour chauffer et ainsi causer une coagulation du tissue dans le but de détruire un cancer qui y serait présent. C'est notamment ce qui est fait dans le cas de l'œsophage de Barrett, un précurseur du cancer de l'œsophage. Le problème de ces thérapies est qu'il est très difficile de connaître la profondeur de la coagulation causée par le traitement. Puisque les résultats de ces thérapies sont très peu reproductibles, il existe des risques de surexposition ou de sous-exposition. Une surexposition peut avoir des conséquences diverses incluant des complications necessitant une chirurgie alors que pour une sous-exposition, le traitement devra être répété, impliquant plusieurs chirurgies.

Pour répondre à cette problématique, plusieurs techniques capables d'identifier la coagulation des tissues ont été développées. Par exemple, la tomographie par cohérence optique (Optical Coherence Tomography ou OCT) est une technique d'imagerie non invasive permettant d'imager la structure des tissues biologiques sur quelques millimètres de profondeur avec une résolution aux alentours de 1-15 micromètres. Elle est d'ailleurs utilisée dans le diagnostic de l'œsophage de Barrett. Elle est aussi capable d'observer plusieurs changements dans le tissue lorsque celui-ci coagule. En l'occurence, le bruit de tavelure ou «speckle pattern» visible à l'OCT subit un changement dans le temps durant la coagulation du tissue avant de se stabiliser une fois que la coagulation est complétée.

Ce changement peut être utilisé pour suivre la coagulation du tissue. Pour y parvenir, un coupleur à double gaine (DCFC, de l'anglais Double-Clad Fiber Coupler) a été utilisé pour combiner l'imagerie OCT et le traitement laser au sein d'une seule fibre à double gaine (DCF, de l'anglais Double-Clad Fiber) garantissant la superposition des deux modalités. Un système a été bâti dans le but de permettre l'imagerie OCT et la thérapie laser par coagulation thermique simultanément. La corrélation de second-ordre a été utilisée sur l'image OCT pour quantifier le changement du patron de tavelure.

Grâce à ce système, il est possible de contrôler la profondeur du traitement laser avec un arrêt automatique lorsque cette profondeur est atteinte. Notre technique a été appliquée avec succès en temps réel à des muscles de rat ex-vivo et nos résultats ont été confirmés par histologie.

Notre algorithme comprend aussi une correction du bruit sur le calcul de la corrélation, permettant un suivi en présence d'un rapport signal sur bruit (SNR, de l'anglais signal to

noise ratio) réduit. Ceci est essentiel, car un tissue biologique coagulé atténue bien plus la lumière, réduisant le SNR sous la zone coagulée. De plus, afin de corriger la décorrelation causée par le mouvement du patient ou de l'opérateur, une correction pour le mouvement a été implémentée. Cette correction utilise la corrélation calculée sur une partie du tissu non affectée par le traitement pour quantifier le mouvement et appliquer un ajustement à la corrélation.

Ce facteur de correction a été trouvé à partir d'une simulation du signal OCT en présence de coagulation. Cette simulation nous a aussi permis de mettre en évidence la différence entre une décorrélation induite par coagulation et par mouvement. Cette différence pourrait être exploitée pour différentier la coagulation du mouvement à partir de la corrélation. Nous n'avons toutefois pas réussi à appliquer cette approche en laboratoire. De plus, cette simulation nous a permis d'entraîner une intelligence artificielle exploitant un réseau de neurone pour reconnaître la coagulation du tissue. Malheureusement encore, nous n'avons pas réussi à appliquer cette technique en laboratoire.

En résumé, ce mémoire porte sur l'utilisation du patron de tavelure d'OCT pour le suivie de la thérapie laser par coagulation thermique. Cette approche permet le contrôle de la profondeur de traitement et est compatible avec les technologies de cathéters actuelles.

ABSTRACT

Laser therapy is a technique exploiting interaction between light and biological tissues for the treatment of illnesses. One of its variations is thermal coagulation where the energy of the light is used to heat up the tissue and cause thermal coagulation in order to kill cancerous cells. Among other applications, it is used in the treatment of the Barrett's esophagus, a potential precursor to esophageal cancer. The challenge of such a therapy is controlling the depth of the induced thermal coagulation. There is a risk of either overexposing or underexposing the tissue to laser light. In the former case, we cause more damage than necessary; in the latter case, we miss the targeted pathology, given it a chance to persist.

Because of this issue, several coagulation-monitoring methods have been proposed. A few of those techniques are based on optical coherence tomography (OCT), a non-invasive optical technique capable of imaging tissue structures with a typical depth of field of a few millimeters and a depth resolution ranging from 1 to 15 microns. This allows for the observation of changes during the coagulation process. Among those changes, is the variation of speckle pattern as the tissue is heated, before stabilizing once the tissue is fully coagulated. OCT has also been proposed as a diagnostic tool for Barrett's esophagus, making it an ideal candidate to perform both identification of the lesion and monitoring of the treatment.

The variation of the speckle pattern has already been suggested to monitor the progression of coagulation, but, to our knowledge, it was never demonstrated in real time. Two issues remain. First, the ability to concurrently obtain images and apply the laser therapy, and second, a computational tool which calculates speckle decorrelation in real time. To accomplish the first challenge, a double-clad fiber coupler (DCFC) was used to combine both OCT imaging and laser therapy through a single double-clad fiber (DCF) for co-registered imaging and therapy. In parallel, the second-order correlation function was used to quantify the change in speckle pattern and allow rapid monitoring of the coagulation.

Our system allows for controlled thermal coagulation depth with the automatic stop of the therapy laser. It was tested on rat muscle in real time with results confirmed by histology.

The algorithm we developed includes noise and motion correction. During coagulation, the attenuation coefficient of the treated tissue increases, attenuating more light, thus lowering the signal-to-noise ratio (SNR) with depth. The noise correction allows for the continuous monitoring at those depths, despite the low SNR. Further correction was necessary as in-vivo monitoring involves motion, either induced by the breathing patient, the operator or the device itself. In order to not induce a bias by the motion on the correlation, a motion correction

algorithm was implemented. The method calculates the motion-induced decorrelation locally in an untreated region of the sample, then applies the appropriate correction globally.

The correction factor was established through a simulation of the OCT signal in the presence of coagulation. This simulation also allowed us to notice the difference in speed between the coagulation and motion-induced decorrelation. This difference could be exploited to differentiate coagulation from motion in the decorrelation value. Unfortunately, we have not succeeded in finding a method that worked experimentally. The coagulation simulation was also used to train a neural network of an artificial intelligence as another monitoring method. Again, however, we have yet to manage to apply the technique on experimental data.

To sum up, the use of OCT speckle was studied as a way to monitor in real time the thermal coagulation depth of laser therapy. The propose method allows for a coagulation depth control of the treatment.

TABLE OF CONTENTS

DEDICATION iii

ACKNOWLEDGEMENTS iv

RÉSUMÉ v

ABSTRACT vii

TABLE OF CONTENTS ix

LIST OF TABLES xi

LIST OF FIGURES xii

LIST OF SYMBOLS AND ACRONYMS xv

CHAPTER 1 INTRODUCTION 1
- 1.1 Problematic 1
- 1.2 Objective 1
- 1.3 Dissertation outline 2

CHAPTER 2 LITERATURE REVIEW 3
- 2.1 Laser Therapy 3
- 2.2 Optical Coherence Tomography 7
- 2.3 Speckle 9
- 2.4 Setup for Bi-Modality 11
- 2.5 Monitoring Laser Therapy 11

CHAPTER 3 PRIOR WORKS 13
- 3.1 Software Development 13
- 3.2 M-Mode Scans Set-Up 15
- 3.3 B-Scan Set-Up 16

CHAPTER 4 ARTICLE 1: REAL-TIME CO-LOCALIZED OCT SURVEILLANCE OF LASER THERAPY USING MOTION CORRECTED SPECKLE DECORRELATION 19

4.1 Introduction 20
4.2 Theoretical model 21
4.2.1 Speckle decorrelation during coagulation 21
4.2.2 Noise correction 24
4.2.3 Motion correction 26
4.3 Materials and methods 27
4.3.1 Experimental setup 27
4.3.2 Software 29
4.3.3 Histology 32
4.4 Results 32
4.4.1 Noise and motion correction 32
4.4.2 Distinguishing coagulated from coagulating tissues 36
4.4.3 Monitoring in real-time 39
4.5 Discussion 40
4.6 Conclusion 43
4.7 Appendix A - Speckle simulation 44

CHAPTER 5 ALTERNATIVE METHODS AND OTHER FINDINGS 48
5.1 Coagulation-Induced Speckle Decorrelation 48
5.1.1 Chosen Approach 48
5.1.2 Results 50
5.2 Neural Network 54

CHAPTER 6 GENERAL DISCUSSION 56
6.1 Signal Treatment 56
6.2 Imaging System 57
6.3 Sample 58

CHAPTER 7 CONCLUSION AND RECOMMENDATIONS 59
7.1 Summary of Works 59
7.2 Signal Treatment 59
7.3 Therapy Laser 59
7.4 Outlook 60

REFERENCES 61

LIST OF TABLES

Table 4.1	Characteristics of the three system modes	31
Table 4.2	Speckle simulation parameters	47
Table 5.1	Coefficients A and B for varying motion.	52
Table 5.2	Coefficients A and B for varying coagulation.	53

LIST OF FIGURES

Figure 2.1 None radiative light and biological interaction depending of power density and exposure time. Reproduced with permission from [1]. 4

Figure 2.2 Absorption coefficients of the main absorbers in biological tissues. Reproduced with permission from [1]. 5

Figure 2.3 In-vivo finger pad as seen in OCT imaging. 7

Figure 2.4 Diagram of a basic OCT system. 8

Figure 2.5 Typical speckle pattern of an OCT image. 10

Figure 3.1 Different steps of contrasting coagulated tissue. The first image is an OCT B-scan of a biological sample while being coagulated by a therapy laser. The second image corresponds to the calculated $g^{(2)}$ while the third is the $g^{(2)}$ corrected for noise. Color bar indicates $g^{(2)}$ value. . . 14

Figure 3.2 Simulation of the portion of coagulation tissue in the sample. On the left, we have the end result with the color bar indicating the damage fraction of the Arrhenius equation. The tissue is considered coagulated for 95% cells dead. On the right, we have the progression of coagulation depth in time. 15

Figure 3.3 $g^{(2)}$ of a beef muscle being coagulated by a CW therapy laser at 150 mW. The Figure shows a series of M-mode scans where each column represent one measure as time progress. 16

Figure 4.1 Overview of the $g^{(2)}$ calculation. Each pixel of the $g^{(2)}$ image (right) is calculated from two ensembles of intensity data points, each ensemble comprising several pixels in z, x and among Δt B-scans in time. The two ensembles are delayed in time by τ. 24

Figure 4.2 Lookup table used for motion correction created from the simulation of coagulation- and motion-induced decorrelation. The vertical axis represents coagulation-induced decorrelation while the horizontal axis represents motion-induced decorrelation. The correction method is as follows: $\tilde{g}^{(2)}_{nc}$ is calculated in an untreated region of the tissue to quantify motion. In step 1. we search for $\tilde{g}^{(2)}_{nc}$ in the first row of the table to determine the motion column index. In step 2. we find the $g^{(2)}_{nc}(x)$ to be corrected for motion in that column and finding its row index. In step 3. we find the $g^{(2)}_{nc\&mc}(x)$ that corresponds to the first value in that row. 28

Figure 4.3 Setup used to obtain co-localized imaging and therapy. 29
Figure 4.4 Setup used to hold and vibrate sample during experiments. 30
Figure 4.5 Data process steps for real-time monitoring. 32
Figure 4.6 Estimated SNR vs. noise intensity calibration curve. 33
Figure 4.7 $g^{(2)}$ before (circle) and after (asterisk) noise correction for low SNR, $R = 9.50dB$, (dark blue) and high SNR, $R = 15.91dB$, (light blue) values. Color palette from [2]. 34
Figure 4.8 (a) Validation of the simulation and motion emulation. $g^{(2)}$ of speckle for simulated (yellow) and experimental (orange) tissue coagulation. Dashed lines represent the data without added motion, both lines are overlapping. Solid lines show $g^{(2)}$ with motion-induced decorrelation added to the coagulation-induced decorrelation. Motion was induced by digitally shifting one of the ensembles by 1 pixel. The figure confirms that motion-induced decorrelation affect simulated and experimental coagulation-induced decorrelation in the same way. (b) Experimental results of the motion correction procedure. $g^{(2)}$ during coagulation (pink curves) and after full coagulation (purple curves), with (dashed curves) and without (solid curves) motion correction. Color palette from [2]. 35
Figure 4.9 $g^{(2)}$ for τ ranging from 10 ms to 40 ms (from dark to pale blue) during laser exposure. From left to right, vertical dashed lines indicate when the laser is turned on, the end of thermal expansion, and when we estimate coagulation to be complete. Color palette from [2] 37
Figure 4.10 Processing steps during Retrospective Diagnostic mode. (a) OCT structural image during therapy, (b) corresponding $g_n^{(2)}$, (c) corresponding $g_{nc}^{(2)}$, and (d) overlay of the OCT intensity (encoded in the luminance) and $g_{nc}^{(2)}$ encoded in the hue of a perceptually uniform isoluminant color map [3]. Scale bars are 0.5 mm. 38
Figure 4.11 Progression of the coagulation highlighted by the correlation of the speckle pattern after 0.5, 1.5, 2.5 and 3.5 seconds of exposure by 10 mJ pulses therapy laser at 100 Hz. Scale bars are 0.5 mm. 38
Figure 4.12 Highlighted coagulation of a rat tongue in the presence of vibration (a) without motion correction and (b) with motion correction compared to (c) the histology section. Red markers of identical lengths are placed on each image to facilitate comparison. Scale bars are 0.5 mm. 39

Figure 4.13 Comparison of varying targeted coagulation depths and motion. The coagulation is highlighted by decorrelation map in color while the red bar shows the depth that was targeted. Scale bars are 0.5mm. 39
Figure 4.14 Highlighted coagulation during laser therapy was automatically stopped when the targeted depth was reached with histology comparison and OCT tomogram for comparison. The red bar shows the targeted depth. Scale bars are 0.5 mm. 40
Figure 5.1 $g^{(2)}$ for simulated speckle patterns. The decorrelation was induced by a change in reflectivity, in orange, a change in position, in blue, and a uniform motion of the scatterers, in purple. 51
Figure 5.2 $g^{(2)}$ of a moving beef muscle in purple and of it coagulating but not moving in blue. 52
Figure 5.3 $g^{(2)}$ of simulated speckle pattern. The speckle pattern was shifted for different amplitude going from lighter blue, for no shift, to a darker blue, for our maximum shift. 53
Figure 5.4 $g^{(2)}$ of simulated speckle pattern. The speckle pattern was shifted for the same amplitude, varying coagulation rate. Going from lighter blue, for the slower rate, to a darker blue, for the fastest. 54

LIST OF SYMBOLS AND ACRONYMS

AI	Artificial Intelligence
CDV	Complexe Differential Variance
DCF	Double-Clad Fiber
DCFC	Double-Clad Fiber Coupler
$\mathcal{F}$	2-D Fast-Fourier Transform
FoV	Field Of View
$g^{(2)}$	Second-Order Correlation Function
galvo	Galvonometer-mounted mirror
HBSS	Hanks' Balanced Salt Solution
IR	Infrared
MC	Monte-Carlo
MCX	Monte-Carlo Extreme
MM	Multimode
NBTC	Nitroblue Tetrazolium Chloride
NURD	None Uniform Rotary Distortion
OCT	Optical Coherence Tomography
OCTA	Optical Coherence Tomography Angiography
NN	Neural Network
PSF	Point Spread Function
ROI	Region Of Interest
SDK	Software Development Kit
SM	Singlemode
SNR	Signal to Noise Ratio

CHAPTER 1 INTRODUCTION

1.1 Problematic

Laser therapy allows for targeted removal or thermal coagulation of tissues through absorption of photons by water and hemoglobin [4–6]. It has found applications in the treatment of epithelial lesions such as Barrett esophagus. Unfortunately, there still lacks an efficient monitoring method for such therapies. Combined with the difficulty of getting reproductive results, there is significant risk of both underexposure and overexposure. Underexposure implies missing the illness allowing for resurgence and necessitating a multitude of therapy. On the other hand, overexposure can lead to complications during surgery. [7–9]

Alternatively, optical coherent tomography (OCT) is a real-time imaging system with an imaging penetration depth of around 2 mm in biological tissues and a depth resolution of around 1 to 15 µm. It can be used in the diagnostic of pathology in the epithelium layer such as Barrett's esophagus. Since tissue coagulation causes changes visible with OCT imaging, the system can be used to monitor the progression of the coagulation depth. [10–13] The challenges that remain, however, is to monitor the coagulation in real time with a method that is compatible with catheter endoscopes.

We propose a real-time coagulation monitoring method based on the use of the second-order correlation function, $g^{(2)}$, on the OCT intensity speckle pattern. The technique allows for perfectly co-registered OCT imaging and laser therapy. A motion correction method is also proposed to have our system more robust to bulk tissue motion.

1.2 Objective

Our objective is to monitor in real time laser-induced thermal coagulation. It can further be divided in the following sub-objectives:

- Develop a system allowing for co-localized laser therapy and imaging that is compatible with catheter-based endoscopes;
- Perform OCT imaging and laser therapy at the same time;
- Achieve coagulation-depth monitoring;
- Compute monitoring algorithm in real time;

- Monitor coagulation in the presence of bulk tissue motion.

1.3 Dissertation outline

In a first step, a literature review is presented. The principles and applications of laser therapy, particularly thermal coagulation, is presented as well as the need for monitoring such techniques. In parallel, we present the principles and applications of optical coherence tomography (OCT), a non-invasive optical imaging method that may be combined with laser therapy. The origin and uses of the speckle pattern will be explained. Since our goal requires combining two modalities, an introduction to double-clad fiber coupler (DCFC) is given. Finally, we will briefly present the different monitoring methods for laser therapy currently available.

Afterwards, the systems and experiments leading to a manuscript will be presented. This section explains how we obtained our first results and how our system was made and improved over the course of the project.

Next, the core of the manuscript will be presented in the form of a submitted article. We go into details about the theory and methodology used. We present our successful tracking of thermal coagulation depth in real time.

After, a section will be dedicated to outstanding issues related to work presented in the manuscript. These include using the $g^{(2)}$ function shape to differentiate coagulation from motion-induced decorrelation. We also explore using neural networks, NN, as an alternative to our current method.

Finally, the discussion and conclusion are presented.

CHAPTER 2 LITERATURE REVIEW

This chapter reviews prior knowledge necessary to understand the content of an original manuscript submitted for publication. It introduces laser therapy, optical coherence tomography (OCT) imaging as well of the origin of speckles, an essential component to our method. Finally, we review the different coagulation monitoring methods available. To avoid repetitions, the theory related to our method is presented in the article, instead of in this current chapter.

2.1 Laser Therapy

Laser therapy describes the interactions of light and biological tissues as a treatment method. The type of non-radiative interaction will depend on how much power is absorbed over which area and time lapse, as well as which optical property is targeted. In the case of photochemical interactions, it will also depend on the targeted chemical properties. Their effects on tissues can be divided in three broad categories: photochemical, photothermal and photomechanical. [14,15] They can have effects on the scale of organelles, cells or tissues. The time lapse of those effects can also be divided between immediate effect, early injury response and late healing response. [14, 16] They can also be summarized like in Figure 2.1 [1], and are described as follows:

- Photochemical: the energy from the light is used as the activation energy to trigger a chemical reaction such as association, decomposition, synthesis, activation and isomerization;
- Photothermal: the energy is converting into heat causing in turn hyperthermia, coagulation, vaporization, carbonization or melting;
- Photoablative: the tissue breaks into pieces at the sudden energy brought by the light;
- Photoplasmic: the electromagnetic field is powerful enough to rip the electrons from their atoms into a free state;
- Photodisruptive: with even more energy, the electromagnetic field becomes strong enough to create a plasma that will in turn causes acoustic shock waves disrupting the tissue structure.

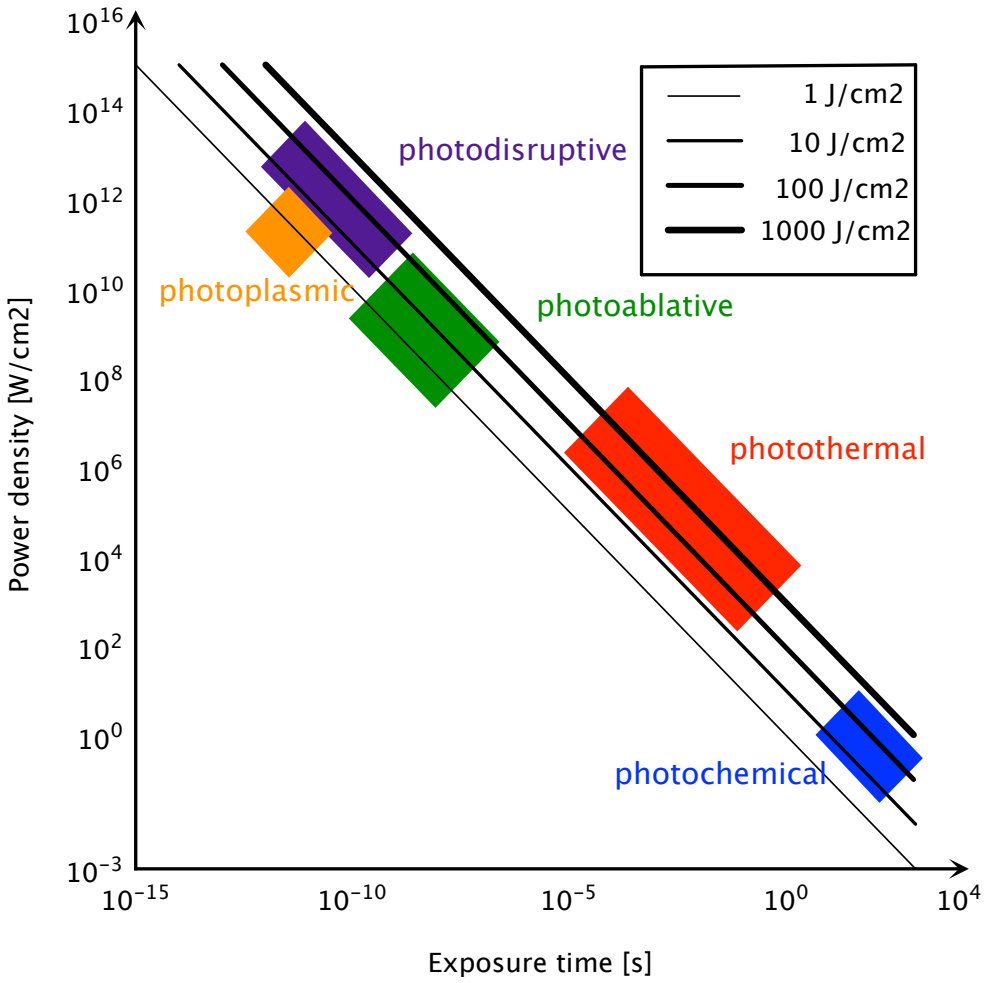


Figure 2.1 None radiative light and biological interaction depending of power density and exposure time. Reproduced with permission from [1].

Power density, however, does not tell the whole story. The absorbed, thus effective, energy will not only depend on the laser power, but on the wavelength and optical properties of the target. Different wavelengths will be absorbed with different coefficients depending on the composition of biological tissues: namely on the concentration of water, hemoglobin and melanin. [4–6] Figure 2.2 [1] shows the absorption spectra for those components. The so-called therapeutic window in the Figure corresponds the range of wavelengths for which light is the least absorbed, thus providing an ideal window for imaging.

On the contrary, when strong absorption is required, it is best to use one of the peaks of absorption. These correspond to the wavelengths used for laser therapy, with the exception of photochemical interaction. Typical wavelengths used for phototherapy are the ultraviolet, UV, light for shallow applications; visible light to selectively target blood vessels; and infrared,

IR, to take advantage of strong water absorption, present almost everywhere in the body. Indeed, the concentration of absorbers will also determine how much light is being absorbed.

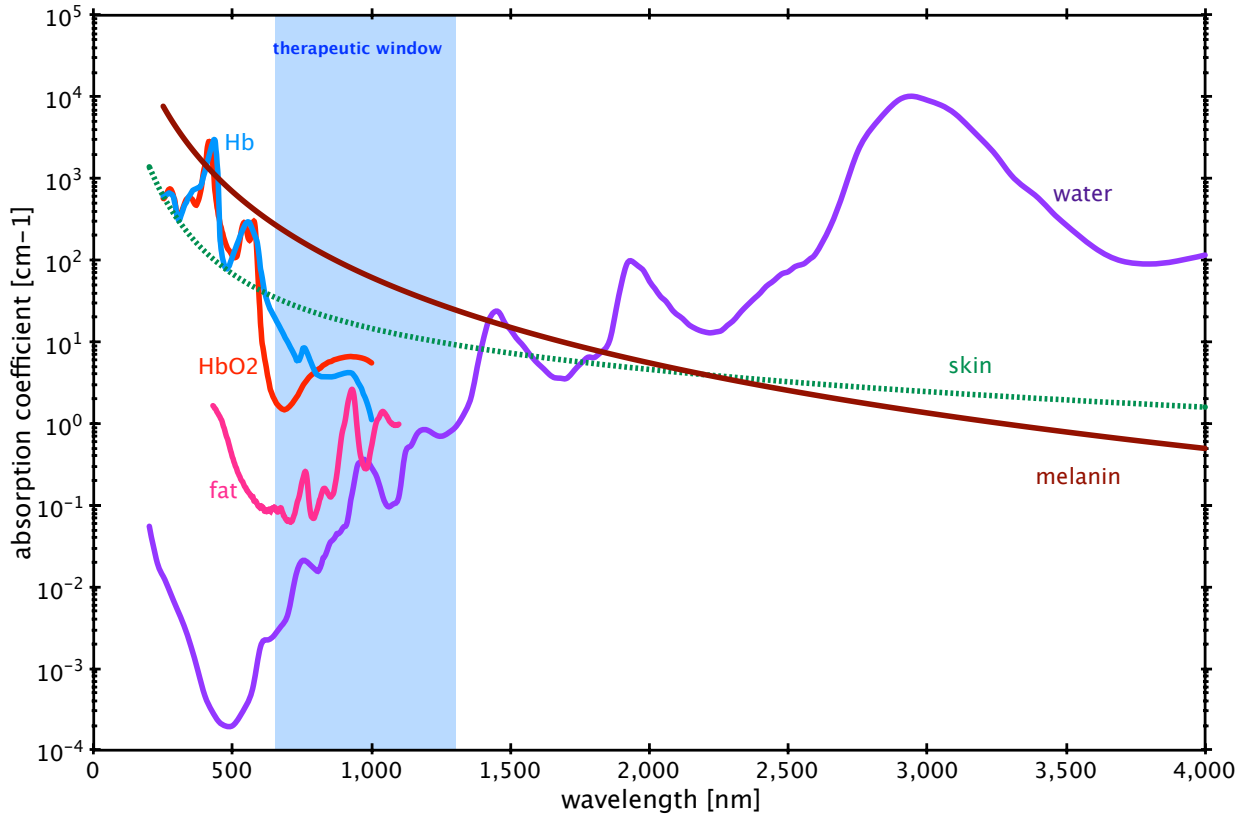


Figure 2.2 Absorption coefficients of the main absorbers in biological tissues. Reproduced with permission from [1].

Exploiting those interactions and absorption peaks allows for exploiting light as a treatment tool. One of the early applications was the removal of tattoos using selective absorption by the ink pigment, but not by the skin. [17] The absorbed energy breaks the pigment which is then evacuated out by the body.

Diseased tissue that needs to be removed can also be targeted in a similar manner. In the case of chemical activation, these interactions can be exploited to activate destructive chemical reactions limiting collateral damage by using the light to activate specific area. Ablation is useful as surgical tools to physically remove the tissue while limiting the damage to the surrounding tissue. [11, 18, 18–22] For example, it can be used to clear the airways of patient with recurrent respiratory papillomatosis. [23, 24]

In our work, we are interested in the immediate photothermal effects on the scale of the tissue.

Thermal coagulation typically happens when the tissue reaches 70 degrees Celsius for a few seconds, depending of the tissue type. [14, 25] It is possible to simulate the process. [26, 27] Indeed, a Monte Carlo (MC) simulator, such as Monte Carlo Extreme (MCX), may simulate where photons are being absorbed the most in our sample. [28] This will depend on the tissue optical properties. The absorbed photons are then converted in a heat source, Q, and the heat equation governed the change in tissue temperature:

$$\nabla \cdot \kappa \nabla \Theta + Q = \rho c \frac{\delta \Theta}{\delta t}, \tag{2.1}$$

where Θ is the temperature of the sample, κ is the thermal conductivity, ρ is the density, c is the specific heat and t is time. [25, 26, 29] The equation can be simulated by converting it into a finite difference equation. [29] How the change in temperature will affect the tissue coagulation can be described by the Arrhenius equation. The equation describes the evolution of most chemical reaction rates, which includes coagulation. In our case, it calculates the concentration of not coagulated cells, C. $C(0)$ being the concentration in the native state and $C(t)$, the concentration at the moment t. There ratio gives us the damage threshold, Ω:

$$\Omega(t) = ln\left(\frac{C(0)}{C(t)}\right) = A\int_t^0 \exp\left(-\frac{E_a}{R\Theta}\right) d\tau, \tag{2.2}$$

where Θ is the temperature (K), A is a frequency factor (Hz) determined experimentally, often associated with the frequency of molecule collisions for other chemical reactions, E_a is the activation energy of the reaction (J/mole) and R is the universal gaz constant. The threshold for tissue necrosis is considered $\Omega = 1$. Both A and E_a are tissue specific and can be found in the literature. Since when the tissue coagulates its optical and thermal properties change, we need to constantly update the MC and heat equation simulation. The cooling effect of blood circulation can be accounted for by adding a term in the heat equation.

Laser induced coagulation has been used to clot bleeding [30] and mark region of interest (ROI) for later biopsy [26]. In our case, we are more interested in using it as a treatment tool.

It is most useful in dealing with precancerous condition in the epithelium layer such as Barrett's esophagus. [8, 31–34] A challenge in using thermal coagulation, however, is getting experimental reproductive results. At the cellular level, no biological sample is exactly the same, causing differences in therapy results despite using the same laser properties. Simulations can make predictions, but those are not accurate enough to avoid either underexposure or overexposure in many cases. Underexposure can lead to a resurgence of the illness and the

need for multiple treatments, increasing both risks and costs. On the other hand, overexposure can lead to complications during surgery. [7–9] This issue justifies the need for efficient real-time methods for monitoring thermal coagulation depth. [10, 13, 30, 35].

2.2 Optical Coherence Tomography

Optical coherence tomography (OCT) is a non-destructive optical imaging method with a depth of field of a few millimeters and an axial resolution around 10 μm. The technique exploits interferometry to map the reflectivity of a sample along the axial direction, providing structural information. The resulting carrot of data is called an A-line. Using a galvanometer-mounted mirror (galvo) in a 4-f system, it is possible to laterally scan the sample to combine A-lines into a 2-D image called a B-scan as shown in Figure 2.3. Using a second galvo mirror to scan the other lateral direction, multiple B-scans can be combined into a 3-D image called a C-scan. [1, 36]

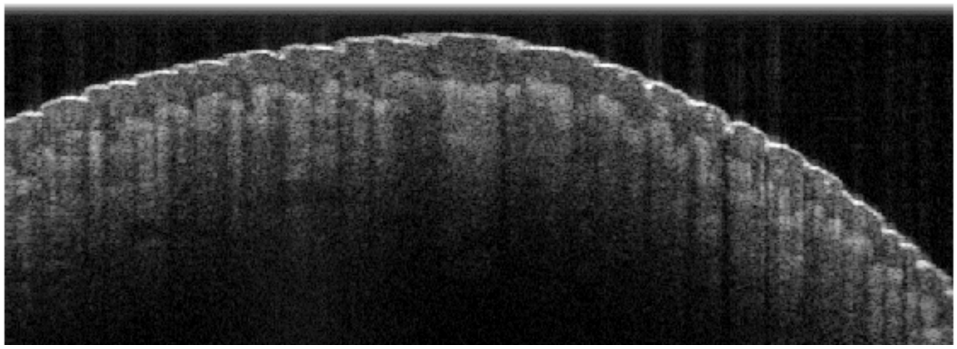


Figure 2.3 In-vivo finger pad as seen in OCT imaging.

Time-domain OCT (TD-OCT) was the technique originally described in the literature. It was, however, soon replaced by a second generation of OCT called Fourier Domain OCT, FD-OCT. This new generation provided better SNR and imaging speed. The two FD-OCT techniques currently used are optical frequency domain imaging (OFDI) and spectral-domain OCT (SD-OCT). The core principle remains the same in both cases.

The technique was originally developed to observe retinal layers in the human eye. It has since then found many applications that are not necessarily limited to biological tissues. Its main applications, however, remains in the angiography of the eye and the observation of epithelial lesions such as the Barrett's esophagus. A typical wavelength used is around 1310 nm, the previous telecom wavelength, to reach deeper structures and because of technologies available at this wavelength. Other wavelengths are also used depending on the biological sample. The 900-1100 nm has low absorption while shorter wavelengths offer higher resolutions.

To image a sample, the technique uses the interference between the light reflected from the sample and a reference arm as shown in Figure 2.4. In TD-OCT, a low coherence source allows for a coherence gating restricted axially by the coherence length of the source. Combined with a moving reference arm, the axial FoV is probed with high spatial resolution, but limited speed and SNR. In FD-OCT, the reference arm is fixed. Coherence gating is achieved through wavelength multiplexing either through a wavelength-swept source (OFDI) or a spectrometer (SD-OCT). A Fourier transform is used in both cases used to extract information about the sample's reflectivity along the axial axis.

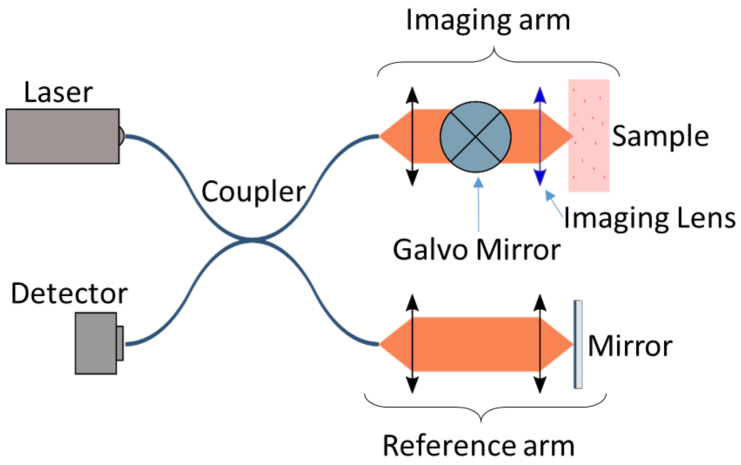


Figure 2.4 Diagram of a basic OCT system.

The use of a broad spectrum leads to problems with dispersion. The dispersion causes a reduction in the axial resolution of the system. There exists, however, techniques to correct for both system induced dispersion [37] and sample induced dispersion [38]. To further improve the signal, multiple types of averaging can reduce the effect of noise on the images. Depending of the goal, the averaging can be done on the OCT spectra, before the Fourier transform, to increase the contrast on low signal structure or on the OCT intensity, after Fourier transform, to reduce the visible noise. [39]

A particularity of OCT is that the lateral resolution, δx, and axial resolution, δz, are independent from one another. The axial resolution depends on the laser source used:

$$\delta z = \frac{2\ln 2}{\pi} \frac{\lambda_0^2}{n\Delta\lambda}, \tag{2.3}$$

where λ_0 the center wavelength $\Delta\lambda$ is the spectral width of the source and n the refractive index of the sample. Thus, the sample also affects the axial resolution. The lateral resolution

depends on the OCT laser beam waist:

$$\delta x = 0.56\frac{\lambda_0}{\mathrm{NA}}, \tag{2.4}$$

where δx NA the numerical aperture of the beam. The NA is mostly a function of the beam waist before the imaging lens and the imaging lens focal length. The useful axial FoV, field of view, is often limited by the attenuation of the sample but can also be limited by the NA for short imaging lens focal length:

$$\mathrm{FoV}_z \approx \frac{0.9n\lambda_0}{\mathrm{NA}^2}. \tag{2.5}$$

The lateral FoV is typically limited by the scanning method. For a galvo mirror scan the FoV is:

$$\mathrm{FoV}_x = 2f\tan(2\theta), \tag{2.6}$$

where f is the focal length of the imaging lens and θ is the maximum deviation angle of the galvo mirror. The two axes different resolution gives us an elliptic Gaussian shaped resolution. This Point Spread Function, PSF, quantify how the different scatterers reflectivity in the sample will affect a single pixel intensity.

2.3 Speckle

As typical for imaging systems using coherent light, speckle patterns are present in OCT imaging, as seen in Figure 2.5. Speckle is a result of the light being reflected from the multitude of scatterers present in the sample. It can be modeled as a sum of random phase vectors. This implies that the probability density function of the sum is a Gaussian random variable in the complex field centered around zero [40]:

$$p_{\Re,\Im}(\Re,\Im) = \frac{1}{2\pi\sigma^2}exp\left(-\frac{\Re^2+\Im^2}{2\sigma^2}\right), \tag{2.7}$$

where $\Re$ and $\Im$ are the real and imaginary part respectively of the speckle signal and σ^2 is the variance of both the real and imaginary parts of the signal. This equation also represents the signal for a complex white noise that is present in OCT images that are added to the OCT complex tomogram. The amplitude of the sum, however, follows a Rayleigh probability density function and thus the intensity, the square of the amplitude, follows an exponential

distribution [40]:

$$p_I(I) = \frac{1}{\overline{I}} exp\left(-I/\overline{I}\right), \tag{2.8}$$

where I is the speckle intensity and $\overline{I}$ is the expected intensity.

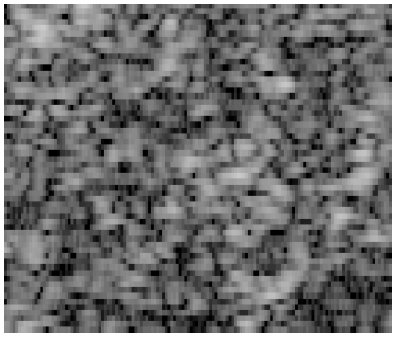


Figure 2.5 Typical speckle pattern of an OCT image.

Since the Point Spread Function (PSF) of the OCT is often a little larger than the OCT image pixel size, OCT speckles are slightly correlated spatially, creating the pattern. [41] Furthermore, the pattern will change in time if the scatterers move.

Though considered detrimental to a clean image of the tissue structures, speckle pattern can be exploited to extract information about a sample. For example, it is, by exploiting the speckle pattern change in time, that OCT angiography (OCTA) can detect blow flow. [42,43] Speckle has also been used to study the scattering coefficient of homogenous samples and the blood coagulation as well as correcting OCT image distortions caused by movement. [44–47] Our interest, however, is in using speckle pattern to monitor tissue thermal coagulation. [12, 13, 35, 48]

Interestingly, like speckle noise, shot noise can be modeled as a sum of random phase vectors. This sum is added to the speckle signal resulting in the noisy signal measured by the OCT. An important difference is that they have no correlation in space or time. The speckle size will be the size of the imaging system pixel and the created speckle pattern of the noise will completely change from one frame to the next.

2.4 Setup for Bi-Modality

In order to monitor our laser therapy with our OCT system, it becomes necessary to combine both modalities. There is a multiple ways of doing this, such as using a dichroic mirror to overlap two laser beams of different wavelengths. [12] Ideally, a solution easily implementable in the clinic is favorable. The solution is found in the use of a double-clad fiber coupler (DCFC) such as the one developed previously by our lab. [26, 35, 49–52]

Fiber couplers are device that allows the light signal guided by a fiber to change fiber. In the case of the DCFC, a double-clad fiber (DCF) is fused with a multimode (MM) fiber. The DCF has a single-mode (SM) core surrounded by a MM cladding. The MM end of the DCFC is used to guide powerful yet incoherent light, such as the therapy laser. The MM is then injected into the inner cladding of the DCF fiber of the DCFC. The SM of the DCFC core can be directly coupled to a 1310 nm OCT system to transport the coherent light to the sample and collect the reflected light back to the OCT device. The DCFC allows for a perfect coregistration of the OCT and therapy lasers.

2.5 Monitoring Laser Therapy

As stated previously, real-time monitoring of laser therapy would be a solution for getting reproductive, and thus reliable, therapy results. A wide variety of solutions have been proposed over the years.

Current non-optical monitoring methods include temperature measurement with thermocouple, allowing only point sampling while resonance thermometry techniques [20, 53] and O-water PET imaging [21] have both limited spatiotemporal resolution and are expensive. Photoacoustic thermography is an alternative optical solution [54, 55] but still has limited resolution, requires the injection of nanoparticles and only provides an indirect measurement of the tissue coagulation.

The solutions that interests us are based on OCT imaging. Tissue coagulation causes visible changes that can be exploited to monitor the thermal coagulation. [10–13, 25] A few of those techniques were originally developed to identify and measure blood flow in OCTA. [42, 43, 56] However, real-time measurement the coagulation-induced changes remains a challenge.

Polarization-sensitive OCT can assess the thermal damage directly, but its contrast is limited to birefringent tissues, such as muscles, cornea and tendons. [19, 57–59] Doppler OCT combined with complex correlation coefficient was also investigated as a way to measure tissue displacement during coagulation. [10, 60–62] Similarly, complex differential variance

(CDV) has been employed with success to differentiate coagulated tissues. [12, 13, 63] These techniques also either require phase stable systems or phase correction which is difficult to achieve in real time in a clinical setting. A phase correction algorithm has been investigated but remains computationally very expensive for real time implementation.

Intensity based methods are probably more suited for real-time applications. They include intensity variance [48], intensity correlation [56] and measuring the change in scattering properties. [11] The last method, however, remains limited to tissue with no visible structure and as yet to be done in real time.

In this work, the second-order correlation function was chosen for its stronger robustness to noise. [64] The noise robustness compensates for the loss in SNR under coagulating tissue, increasing the maximum monitoring depth. It also provides fixed expected values for fully correlated or decorrelated intensity speckle pattern as opposed to variance. This allowed us to developed an automatic detection system of the coagulation. Furthermore, the function relies on the intensity of the signal instead of the complex amplitude processing required with CDV, the signal processing complexity is thus significantly reduced, allowing for real-time monitoring.

The second-order correlation function of the light electromagnetic corresponds the correlation function of the light intensity, as opposed to the light electromagnetic amplitude. The exact signal processing is presented in the Theory section of Chapter 4.

CHAPTER 3 PRIOR WORKS

This section is dedicated to the work that lead to the experiments presented in Chapter 4. We started by developing the software necessary to the coagulation detection. Next, we developed our first rudimentary OCT system functioning only in M-mode scans. Finally, we introduce our final set-up.

3.1 Software Development

To accelerate the development of an algorithm, we began with data from a previous experiment performed by our group [12]. In these experiments, an Infrared (IR) therapy laser co-registered using a dichroic laser was used to coagulate biological tissue while OCT B-scans were taken. This allowed us to start working on the coagulation detection software. The goal was to reproduce previous results based on the Complexe Differential Variance (CDV) in a more efficient way.

The first attempts were performed before the literature review was completed and were unsuccessful. My co-director then recommended using the $g^{(2)}$, the second-order correlation function, as well as using a novel noise correction. It was during this period that the noise calibration method was developed. The decorrelation map in Figure 3.1 was then obtained. We can see in the Figure how the $g^{(2)}$ can be used to contrast the coagulated tissue at the center. Furthermore, the noise correction removed the bias introduced by the noise, showing the tip of the coagulation depth. The tools to monitor the thermal coagulation were ready.

Through the use of a coagulation simulation, attempts were made in developing a theoretical model in order to estimate the necessary laser powers for our experimental set-up and having a reference to which compare our future experimental results. Our simulation was mainly based on a previous work by our group [26]. In the end, the simulation was not used to produce results as much as to learn about the different processes involved during coagulation. The next section provides an overview of the algorithm.

The simulation uses a combination of Monte Carlo simulation, finite difference heat equation and finite difference Arrhenius equation to calculate the different processes involved during coagulation described in the literature review. Monte Carlo Extreme, MCX, a software based on GPU computing, was used to determine the absorbed light energy per unit of volume across the sample. The heat equation, Equation 2.1, was simulated using a finite difference implicit method, among other methods, for its rapid computing and accuracy. [29]

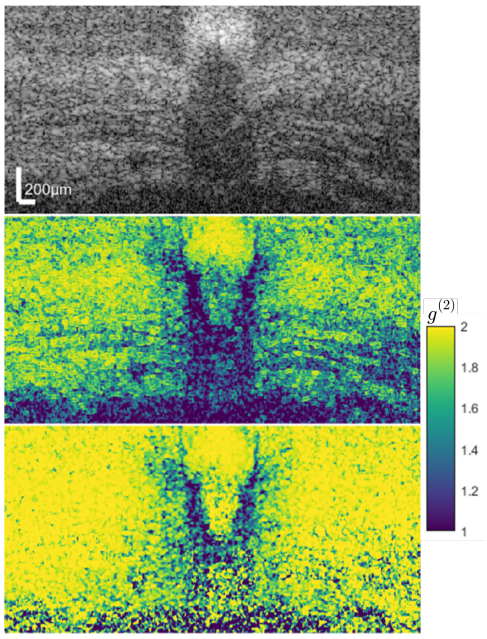


Figure 3.1 Different steps of contrasting coagulated tissue. The first image is an OCT B-scan of a biological sample while being coagulated by a therapy laser. The second image corresponds to the calculated $g^{(2)}$ while the third is the $g^{(2)}$ corrected for noise. Color bar indicates $g^{(2)}$ value.

By assuming a static laser source, which can be a valid approximation, cylindrical coordinates were used to simplify and accelerate computing. The boundary conditions in the tissue were considered at a constant temperature, making them a perfect heat sink. This approach is valid because our simulated space was wide enough that the heat from the laser never reached these boundaries. The tissue-air boundary condition was modelled as a convective boundary [26]. Equation 2.2, the Arrehnius equation, was also simulated with a finite difference implicit method. An example of results are shown in Figure 3.2.

We had hoped that the simulation would serve us as a theoretical model. Unfortunately, since we were not sure about the correct coefficient value to properly modeled the tissue-air surface as a convective boundary, the general incertitude on most of the optical and thermal properties and the absence of a proper validation method, it was never used as such. However, a similar approach was previously validated before. [26,27] It still gave us an idea of the laser power necessary for our tests and the dynamic between laser power and heat dissipation involved in the process.

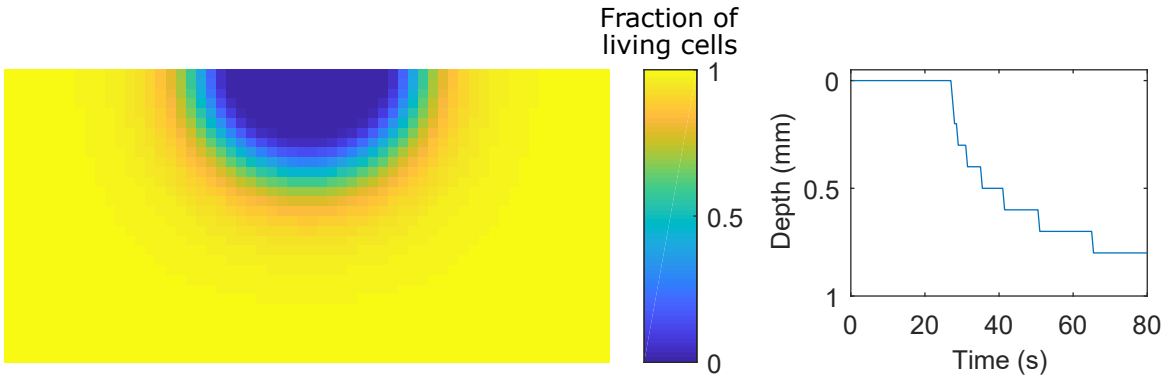


Figure 3.2 Simulation of the portion of coagulation tissue in the sample. On the left, we have the end result with the color bar indicating the damage fraction of the Arrhenius equation. The tissue is considered coagulated for 95% cells dead. On the right, we have the progression of coagulation depth in time.

3.2 M-Mode Scans Set-Up

Our first set-up was made with a commercial MEMS-VCSEL swept laser OCT at 1310 nm, Thorlabs SL1310V1, and a CW 532 nm laser, the Verdi 10W, as therapy laser. The OCT came with a Thorlabs imaging head and software. This brought two issues.

The first was that the laser power necessary for inducing thermal coagulation was above the damage threshold of the OCT imaging head. The optics in the head would thus have been damaged by the therapy laser. The second issue was that the Thorlabs software could not save the OCT intensity data necessary for our algorithm to work. Instead, it could only save either the raw OCT data or the final images. We had yet to produce that software necessary to analyse raw OCT data.

To solve the imaging head issue, the imaging lens was replaced by an uncoated collimator and lens. No mirror galvo were used and thus it was not possible to do B-scans. Since it was the beginning of the project, no alternative to the Thorlabs program existed. It was instead opted to continue using the Thorlabs program but plug the fiber in our own imaging head. This allowed us to do M-mode scans by taking B-scan with the Thorlabs software and saving the images. The set-up was far from being ideal, but it gave us preliminary results.

To combine the OCT and therapy lasers, a DCFC from Castor Optics was used. The double-clad end was plugged directly in the OCT laser and our imaging head. The DCFC introduced a ghost image as explained in [35], but since the artifact did not overlap with the region of interest in our OCT image, our results were not affected by it. A fiber was added in the

reference arm to match both arms lengths. At this stage, there was no dispersion correction. The therapy laser was injected into the multimode end of the DCFC. For safety, the whole injection set-up was placed in a closed box.

The first trials were done on beef muscles. The therapy laser was confirmed to be more than powerful enough to induce thermal coagulation when fired continuously. Multiple measures at different powers were taken. Efforts were made to translate the dB OCT image in a linear intensity scale. The algorithm develops in the previous section was then applied to obtain our first results as displayed in Figure 3.3. We see a decorrelation at all depths appeared after the laser is turned on before it becomes correlated again as the coagulation progress downward.

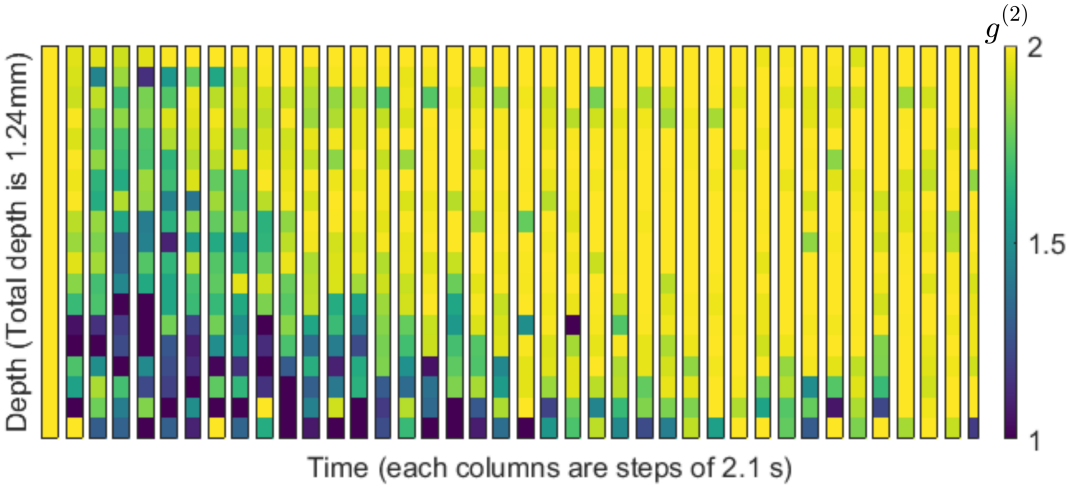


Figure 3.3 $g^{(2)}$ of a beef muscle being coagulated by a CW therapy laser at 150 mW. The Figure shows a series of M-mode scans where each column represent one measure as time progress.

Those results were promising. They showed a rapid progression of the coagulation depth before slowing down as it as predicted by our simulation. Other experiments were done with similar success with porcine liver. Attempts were made to cut the samples in half to verify the coagulation depth, but the method was too inaccurate.

3.3 B-Scan Set-Up

Our next generation system objective was to reproduce our previous results with B-scans and calculate $g^{(2)}$ for real time monitoring. To achieve this, a custom imaging head and software were made as described in Chapter 4.

The custom Labview software was made using in part the Alazartech SDK. The developped algorithms previously used, were implemented in Labview.

Since our samples were now scanned, it means that we had to make our therapy laser pulse in synchronization with the B-scan in order to coagulate only the center of the sample. In order to reach higher pulse energy for the therapy laser, a lot of time was past contacting enterprises to find a better suited laser. Sadly, no lasers at a reasonable price allowed for both the fine frequency control of the pulses with high enough energy. The optimal solution would have been to make one ourselves, but that would have been a project in itself. Instead, a galvo mirror was added in the therapy laser injection system described in Chapter 4.

To further improve the OCT image, a splice was done on the DCFC end connected to the OCT. The splice added a single-mode fiber in order to attenuate the ghost image created by the DCFC with some success. The reference arm was spliced in the same way so that both arms kept the same fiber length.

Furthermore, dispersion compensation was added later to the OCT image processing and it greatly improved image quality. Two methods were used. The first was the one suggested in [38]. It was later replaced by a technique developed in our laboratory [37]. The first technique allowed for correcting dispersion induced by the sample. This, however, required to have a clear structure beneath the surface of the sample, which was not the case for most of our sample. The second technique had the advantage of theoretically correcting exactly the system's dispersion. It also allowed us to improve the sampling of our k-clock, further improving our axial resolution. The imaging lens and reference arm positions were also optimized to ensure that the imaging focal point was in the sample. Previously, the axial position of the waist was optimized for the therapy laser, and not for imaging. Since the therapy laser had a different wavelength, it also meant a different waist position. Since we were in a thermal regime, where the coagulated zone is wider than the beam waist, we decided to favor optimizing the waist for the OCT image.

Finally, we searched for an ideal tissue sample: one that would have an adequate absorption coefficient while showing structures observable by OCT. We started using fresh muscles and organs from sacrificed rats from Sainte-Justine Hospital. We worked with pathologists to establish a histology protocol, described briefly in the article, to have a gold standard with which to compare our results. In the end, we settled on using rat muscle around the abdominal area because the different muscle layers were visible on the OCT and the samples retained enough blood to allow for thermal coagulation.

We also considered using freshly sacrificed porcine esophagus, the organ targeted as a potential application. Unfortunately, coagulation on such a sample did not work as OCT and

histology required soaking samples in HBSS in order to preserve proper hydration. However, HBBS diluted the blood, which, combined with a loss of blood pressure after death, hemoglobin was no longer present in high enough quantity to allow for photocoagulation.

CHAPTER 4 ARTICLE 1: REAL-TIME CO-LOCALIZED OCT SURVEILLANCE OF LASER THERAPY USING MOTION CORRECTED SPECKLE DECORRELATION

This article presents the core results from this project. We delve in the details about the use of $g^{(2)}$ to monitor thermal coagulation depth. The theory associated to noise and motion corrections as well as their implementations are explained. The experimental set-up, a custom Labview software, and experimental methodology are also presented. We present our findings on the effects of coagulation, noise correction, tissue motion and corrections on the $g^{(2)}$ function. Finally, we present our results of having successfully controlled coagulation depths validated through histology.

The main author, Raphaël Maltais-Tariant, contributed to 90% of the work. This includes literature research, assembling both the system set-up and writing the software and experimental protocol, performing the experiment, analysing the results and writing the article. Dr. Néstor Uribe-Patarroyo, PhD, and Prof. Caroline Boudoux, ing., PhD, are the principal investigators on this project. They provided advice during its course and contributed to the revision of the article.

Authors: Raphaël Maltais-Tariant, Caroline Boudoux and Néstor Uribe Patarroyo.

Article submitted: Biomedical Optics Express, December 2019

Abstract: We present a system capable of real-time delivery and monitoring of laser therapy by imaging with optical coherence tomography (OCT) through a double-clad fiber (DCF). A double-clad fiber coupler is used to inject and collect OCT light into the core of a DCF and inject the therapy light into its larger inner cladding, allowing for both imaging and therapy to be perfectly coregistered. Monitoring of treatment depth is achieved by measuring the speckle intensity decorrelation occurring during tissue coagulation. Furthermore, an analytical noise correction was used on the decorrelation to extend the maximum monitoring depth. We also present a method for correcting motion-induced decorrelation using a lookup table. Using the value of the noise- and motion-corrected correlation coefficient in a novel approach, our system is capable of identifying the depth of thermal coagulation in real time and automatically shut the therapy laser off when the targeted depth is reached. The process is demonstrated *ex vivo* in rat tongue and abdominal muscles for depths ranging from 500 μm to 1000 μm with induced motion in real time.

4.1 Introduction

Laser therapy allows for targeted removal or thermal coagulation of tissues through light absorption by various absorbers in the tissue, such as water, hemoglobin and other macromolecules [4–6]. It is used in the treatment of epithelial cancerous and pre-cancerous lesions such as Barrett's esophagus [31–33], in eye diseases such as diabetic retinopathy [22, 65–67] and retinal vein occlusion [68, 69] and in respiratory papillomatosis, a viral-induced disease in the upper airway [23, 24]. However, accurate monitoring is essential to avoid over- or under-treatment. Under-treatment requires repeat visits with the associated cost, while overtreatment generally causes complications requiring surgical treatment [7–9]. Such precise monitoring requires real-time imaging techniques capable of resolving the thin epithelial layers (generally a few hundred microns) under treatment. Furthermore, when the target zone is small and presents mostly subsurface features for guidance, properly targeting the therapy can prove challenging unless treatment is guided by cross-sectional imaging.

Current monitoring methods for laser therapy are limited. Ultrasound imaging has been used to monitor photothermal therapy in cancer treatment, but lacks sufficient resolution to accurately assess treatment depth in the epithelial layers of tissue [70]. Photoacoustic thermography [55] also has limited resolution, requires the injection of nanoparticles, and only provides an indirect measurement of the tissue coagulation. Thermal magnetic resonance imaging has been demonstrated for treatment monitoring, but this approach is costly and presents challenges such as motion artifacts and complex procedures for choosing the optimal monitoring parameters [71–73].

Alternatively, optical coherence tomography (OCT) is a cross-sectional imaging technique with a penetration depth of 1–2 mm and a depth resolution of 1–15 μm [36]. It has been used in identifying pathologies in the epithelium layer of different tissues, including some treatable with laser therapy, such as Barrett's esophagus [74–76]. Tissue coagulation produces changes in the acquired OCT tomograms which enable the use of OCT to monitor the progression of the coagulation process and determine treatment depth [10–13, 48, 63, 77].

Several methods have been proposed to guide treatment with OCT. Changes in tissues scattering properties have been exploited, but it tends to underestimate the therapy depth [11,12]. Polarization-sensitive OCT can assess the thermal damage directly, but its contrast is limited to birefringent tissues at baseline, such as muscles, skin and tendons [19, 57–59]. Doppler OCT combined with analysis of the complex correlation coefficient has also been investigated as a way to measure tissue displacement during coagulation [10, 62], however no determination of the level of coagulation of tissue was attempted. An OCT angiography technique

known as complex differential variance (CDV) [42] has been employed with success to differentiate coagulated tissues in laser and radio-frequency therapy [12, 13]. CDV makes use of the complex-amplitude OCT signal, which adds significant complexity to a real-time implementation of the signal processing. Indeed, many clinical systems lack phase stability: the presence of patient motion or the use of endoscopic probes with scanning inaccuracies such as non-uniform rotation distortion make it necessary to implement several steps of phase jitter correction and motion and distortion correction difficult to achieve in real time [13]. To the best of our knowledge, OCT real-time monitoring capable of dynamically controlling the therapy laser when the target treatment depth has been achieved has not been demonstrated.

In this work, we present a system capable of real-time monitoring of the coagulation depth in epithelial tissue compatible with catheter imaging. A double-clad fiber coupler (DCFC) is used to combine both the OCT and therapy laser in a single double-clad fiber (DCF) for co-registered imaging and therapy [35, 50, 52]. This represents an improvement from Ref. [12], where the two lasers were combined using a dichroic mirror, a configuration appropriate for benchtop validation but impractical for clinical use and incompatible with endoscopic systems. We achieve monitoring using the *intensity* decorrelation of the speckle, which lowers the signal processing complexity significantly compared to the *complex-amplitude* speckle processing required with CDV. Furthermore, novel noise- and motion-correction methods are added to simultaneously extend the maximum monitoring depth and improve system robustness to bulk tissue motion. We implemented these signal processing methods in both post-processing and real time. We demonstrate the use of the developed system in a benchtop configuration for real-time coagulation depth monitoring and targeting, where the system stops the therapy laser automatically when the desired treatment depth has been reached, despite the presence of bulk tissue motion. We validated our approach in *ex vivo* rat tongue and abdominal muscle tissue, with histology confirmation. Our approach opens the possibility for future real-time image-guided laser therapy with high spatial and temporal resolution through a single fiber endoscope.

4.2 Theoretical model

4.2.1 Speckle decorrelation during coagulation

Speckle results from the interference of the coherent light reflected or back-scattered off the scatterers present within a turbid sample. In OCT, a given sub-resolution spatial distribution of scatterers with its associated scatterer size and refractive index yields a specific speckle pattern provided there are no intrinsic —such as diffusion— or extrinsic —such as bulk tissue

motion— mechanisms affecting their configuration state [40]. However, as tissue undergoes photocoagulation, proteins denaturate, producing a change in the refractive index distribution and, therefore, a change in the coherent sum of individual back-scattered contributions resulting in a temporal evolution of the speckle pattern seen in the tomogram [48, 60, 62, 63]. Lo et al. observed that these variations slow down once the tissue has fully coagulated [12]. By monitoring the speckle pattern dynamics as it transitions *from static* (before coagulation), *to dynamic* (during active coagulation) and *back to static* (after coagulation), it becomes possible to determine the state of each part of the tissue during therapy [12].

The quantitative analysis of the speckle fluctuations can be performed by determining the temporal decorrelation of the OCT signal. When relying on the intensity of the signal, the second-order autocorrelation function $g^{(2)}$ is generally used to quantify the decorrelation. In what follows, we describe how $g^{(2)}$ can be used to create a map of the OCT signal decorrelation across the field of view. We define a discrete coordinate system (z, x, y) defining the axes in depth, in-plane lateral location, and out-of-plane lateral location, respectively. In the following, we do not consider the out-of-plane dependency, unless otherwise specified.

The second-order autocorrelation function calculates the time-delayed correlation of the intensity of an ensemble at a time difference τ and can be written as [64, 78]

$$g^{(2)}(\tau) = \frac{\langle \int I(t) I(t+\tau) dt \rangle}{\int \langle I(t) \rangle \langle I(t+\tau) \rangle \, dt}, \tag{4.1}$$

where I is the intensity and $\langle \cdot \rangle$ denotes an ensemble average. Since our OCT system acquires a finite, discrete number of B-scans ΔT, we convert the integration into a summation over the entire acquisition. Furthermore, the intensity of the system will be a function of depth, z, and lateral position, x,

$$g^{(2)}(z, x, \tau) = \frac{\left\langle \sum_{t=0}^{\Delta T - \tau} I(k, l, t) \odot I(k, l, t+\tau) \right\rangle_{kl}}{\sum_{t=0}^{\Delta T - \tau} \langle I(k, l, t) \rangle \langle I(k, l, t+\tau) \rangle_{kl}}, \tag{4.2}$$

where ΔT is the number of available B-scans to calculate the correlation, $\odot$ is the Hadamard product, and $\langle \cdots \rangle_{kl}$ represents an ensemble average of $I(k, l, t)$ in the k and l indices centered around (z,x). An precise definition of the ensemble will be given in Eq. 4.4. This is a direct translation of the estimation of the autocorrelation function for a *stationary* process. However, as explained above, during tissue coagulation the tissue transitions through different states and therefore the acquired signal corresponds to a *dynamic* process. In a dynamic process, $g^{(2)}$ depends not only on τ but also on t. In Eq. (4.2) we therefore limit the temporal extent of the summation to allow us to calculate a time-dependent correlation assuming the

sample is in the same state inside a limited time interval. If we define Δt as the number of B-scans used for the *instantaneous*, estimation of the autocorrelation at time t, Eq. (4.2) becomes

$$g^{(2)}(z,x,t,\tau) = \frac{\left\langle \sum_{m=t}^{\Delta t} I(k,l,m) \odot I(k,l,m-\tau) \right\rangle_{kl}}{\sum_{m=t}^{\Delta t} \langle I(k,l,m)\rangle \left\langle I(k,l,m-\tau)\right\rangle_{kl}}. \tag{4.3}$$

Notice that we use $m-\tau$ for our second ensemble since, for the calculation of the correlation in real time, we only have access to the B-scans preceding t. To simplify the notation, we drop the summation and change the definition of ensemble to

$$I_{ens}(z,x,t) \equiv \{I(k,l,m)\}, \text{ for } \begin{cases} \forall k & \in & \{z, z+1, \cdots, z+\Delta z\} \\ \forall l & \in & \{x, x-\Delta x+1, \cdots, x+\Delta x\} \\ \forall m & \in & \{t-\Delta t, t-\Delta t+1, \cdots, t\} \end{cases}, \tag{4.4}$$

where $I(k,l,m)$ is the intensity of the pixel at depth k, lateral position l and time m; and $\{\cdots\}$ denotes the concatenation of the argument into an ensemble. The ensemble $I_{ens}(z,x,t)$ encompasses all pixels at depths z to $z+\Delta z$, lateral positions x to $x+\Delta x$ and times t to $t-\Delta t$. Our time-dependent autocorrelation function becomes

$$g^{(2)}(z,x,t,\tau) = \frac{\langle I_{ens}(z,x,t-\tau) \odot I_{ens}(z,x,t)\rangle}{\langle I_{ens}(z,x,t-\tau)\rangle \langle I_{ens}(z,x,t)\rangle}, \tag{4.5}$$

where the bracket $\langle\cdots\rangle$ denotes an ensemble average implemented as $\sum_{klm}$. Decorrelated speckle patterns will have $g^{(2)} \to 1$ while correlated patterns will have $g^{(2)} \to 2$ for speckle with unity contrast, as is the case of OCT [79]. These theoretical values for $g^{(2)}$ are reached for infinitely large ensembles. Since the ensembles considered here are small, we define a normalized second-order autocorrelation function $g_n^{(2)}$ that accounts for non-unity contrast as

$$g_n^{(2)}(z,x,t,\tau) = \frac{g^{(2)}(z,x,t,\tau)-1}{g_0^{(2)}(z,x,t,\tau)-1} + 1. \tag{4.6}$$

The zero-delay autocorrelation used for normalization $g_0^{(2)}$ takes into account the contrast of the speckle in all the samples used in the calculation of the time-dependent autocorrelation function and is thus a function of τ and t given by

$$g_0^{(2)}(z,x,t,\tau) = \frac{\langle \{I_{ens}(z,x,t-\tau), I_{ens}(z,x,t)\} \odot \{I_{ens}(z,x,t-\tau), I_{ens}(z,x,t)\}\rangle}{\langle \{I_{ens}(z,x,t-\tau), I_{ens}(z,x,t)\}\rangle^2}. \tag{4.7}$$

The term $\{I_{ens}(z,x,t-\tau), I_{ens}(z,x,t)\}$ is a concatenation of the two ensembles $I_{ens}(z,x,t-\tau)$ and $I_{ens}(z,x,t)$. We ignore any dependency of the calculated value of the autocorrelation function with the ensemble size as we do not compare results among different ensemble

sizes [79]. During therapy, we calculate $g_n^{(2)}$ for all positions in the OCT tomogram. Fig. 4.1 shows an example for a given value of τ and t. We elaborate on the choice of τ in Sec. 4.4.2. As for Δz, Δx and Δt, a larger ensemble provides a better estimation of the correlation at the cost of resolution in z, x and t.

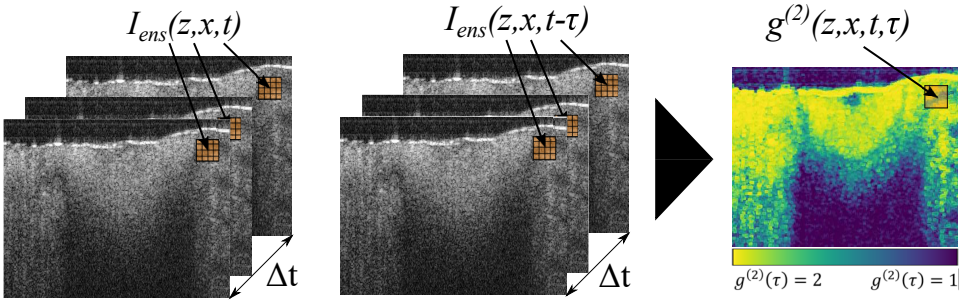


Figure 4.1 Overview of the $g^{(2)}$ calculation. Each pixel of the $g^{(2)}$ image (right) is calculated from two ensembles of intensity data points, each ensemble comprising several pixels in z, x and among Δt B-scans in time. The two ensembles are delayed in time by τ.

4.2.2 Noise correction

Noise, being dynamic in time, will lower the correlation coefficient calculated [64]. This effect becomes significant during coagulation when the SNR decreases, caused by the increased scattering of coagulated tissue, which then limits the maximum possible monitoring depth of the therapy [11,12]. As such, it is crucial to implement noise correction methods that account for these effects. We use a novel analytic correction for the noise-induced decorrelation, as proposed by Uribe-Patarroyo et al. [79], which does not suffer from the loss in temporal resolution of previous corrections [64]. Briefly, the shot noise component in the OCT tomogram can be modeled as an additive white-noise contribution to the complex-valued tomogram [80]. The noisy complex-valued signal G is defined as $G = S + N$ where S is the noiseless signal and N is the noise. The noisy signal intensity I is therefore $I = |S + N|^2$. We also define a noiseless signal intensity $T = |S|^2$. Temporarily replacing the indices $(z, x, t-\tau)$ and (z, x, t) with $_1$ and $_2$, respectively, it is possible to write the second-order autocorrelation function of the noisy signal as

$$g^{(2)}(z,x,t,\tau) = \frac{g_c^{(2)}(z,x,t,\tau) + G}{1+G}, \tag{4.8}$$

$$g_0^{(2)}(z,x,t,\tau) = \frac{g_{c,0}^{(2)}(z,x,t,\tau) + 2G_0}{1+G_0}, \tag{4.9}$$

where

$$g_c^{(2)}(z,x,t,\tau) = \frac{\langle T_1 T_2 \rangle}{\langle T_1 \rangle \langle T_2 \rangle} \tag{4.10}$$

is the second-order autocorrelation function in absence of noise, and $g_{c,0}^{(2)}$ is defined in a similar fashion. The parameter G is given by the average SNR of the ensembles, written as R:

$$G = \frac{1 + R_1 + R_2}{R_1 R_2}, \tag{4.11}$$

$$G_0 = \frac{1 + 2R}{R^2}, \tag{4.12}$$

where

$$R_j = \frac{\langle I_j \rangle}{\langle |N|^2 \rangle} - 1, \tag{4.13}$$

and R denotes the SNR of the two ensembles $\{I_1, I_2\}$. It is straightforward to express $g_c^{(2)}$ $[g_{c,0}^{(2)}]$ as a function of $g^{(2)}$ $[g_0^{(2)}]$ and obtain noise-corrected versions of Eq.(4.5). The normalized and SNR-corrected autocorrelation function becomes

$$g_{nc}^{(2)}(z,x,t,\tau) = 2\frac{g^{(2)}(z,x,t,\tau)[1+G] - G}{g_0^{(2)}(z,x,t,\tau)[1+G_0] - 2G_0}. \tag{4.14}$$

DCF is known to have some level of cross-talk between the single-mode core and inner cladding, which results in ghost images and/or increased noise floor. For this reason, we decided not to rely on the noise floor determined by blocking the sample arm [35]. We thus developed a calibration procedure to accurately determine the noise level, using a tomogram acquired prior to the start of the coagulation process. An additional advantage of this method is the possibility of estimating the SNR for data for which the noise floor is unknown. First, we assumed that the SNRs of both ensembles are identical, $R_1 = R_2$, which proved to be an excellent approximation. This also implied that $G = G_0$. We also assumed that the noise intensity remains constant for the remainder of the coagulation, and that the SNR will, therefore, only change due to variations in the signal intensity

$$R(z,x,t) = \frac{\langle I_{ens}(z,x,t) \rangle}{\langle |N|^2 \rangle} - 1, \tag{4.15}$$

where $I_{ens}(z,x,t)$ is the I ensemble located at z, x and t, and it is made explicit that N is independent of z, x and t. In order to confirm the linear relationship between the R and $\langle I_{ens} \rangle$, R was estimated for varying $\langle I_{ens} \rangle$ values. More precisely, we estimated the average SNR of the j-th ensemble, $\bar{R}_j$, as a function of its average signal intensity, $\langle I_j \rangle$, for all the ensembles

in the field of view. This calibration was found by solving the optimization problem outlined in Eq. 4.16. For a static sample with no ongoing treatment, the only source of decorrelation will be the noise. We can therefore expect $g^{(2)}_{nc}(\tau > 0) = 2$ and write

$$\underset{\bar{R}_j \in \mathbf{R}_{\geq 0}}{\arg\min} \left| g^{(2)}_{nc}(\bar{R}_j, \tau > 0) - 2 \right| \text{ for } j = 1, \cdots, m, \tag{4.16}$$

m being the total number of ensembles. Since the estimation of $\bar{R}_j$ as a function of $\langle I_j \rangle$ for a single ensemble tends to be inaccurate, ensembles were grouped in M bins: ensembles with similar average intensity were grouped in the j-th bin with average intensity I_j. Considering the full dynamic range of the signal, we equally distributed all ensembles into $M = 100$ bins [thus $j = 1 \ldots 100$ in Eq. (4.16)], and and the optimization problem was solved for each bin. We selected the number of bins by finding a good compromise between an accurate estimation of the SNR and a good resolution on the $\bar{R}_j$ vs. $\langle I_j \rangle$ curve and the time it took to solve all of the optimizations.

The optimization problem itself was solved using a similar approach to the golden-section search method [81]. The function is evaluated at three points, x_1, x_2 and x_3 separated by intervals of Δx. Step one consists of finding the minimum value between the function evaluated at these three points. In step two, we created a new interval of three points separated by $\Delta x/2$ centered around the minimum calculated in step one. The process is iterated until the interval separating the three points is considered small enough. In our case, this value was 1% of $\langle I_j \rangle$. This method was chosen because it was found to converge rapidly with our data; however, in principle, any optimization method can be used as the search space seems to have a single global minimum. The curve is used as a lookup table to calculate $g^{(2)}_{nc}(z, x, t, \tau)$ using the proper SNR value, searched for making use of only the current ensemble intensity at each t.

4.2.3 Motion correction

It is well establish that tissue bulk motion will affect the value of $g^{(2)}$, thereby leading to inaccurate measurements of the coagulation-induced decorrelation. To address this impact, we devised a method based on a lookup table. The two-dimensional table gives the $g^{(2)}_{nc}$ value caused by motion-induced decorrelation on the horizontal axis and by coagulation-induced decorrelation on the vertical axis. Points lying in between the two axes correspond to decorrelation caused by a combination of both coagulation and motion.

The method works as follows. A look-up table $g^{(2)}_{nc}(k, l)$ is created, in which the row index, k, corresponds to the degree of coagulation-induced decorrelation, and the column index, l,

corresponds to the motion-induced decorrelation. The first row $g_{nc}^{(2)}(k=0,l)$ corresponds to the expected value of $g_{nc}^{(2)}$ for untreated tissue and all possible degrees of tissue motion (given by l). For a given experiment, motion is quantified by calculating $g_{nc}^{(2)}$ in an *untreated* section of the tissue, which we denote the *reference* autocorrelation, $\tilde{g}_{nc}^{(2)}$. The value of $\tilde{g}_{nc}^{(2)}$ will be searched for in the first row of the table. The associated column index, l_R, will define the motion-induced decorrelation for all ensembles in the current frame. This is represented as step 1 in Fig. 4.2. In step 2, to correct a given $g_{nc}^{(2)}(x)$, the index k_m having the closest match in the column given by $g_{nc}^{(2)}(k,l_R)$ is found, such that $g_{nc}^{(2)}(x) \approx g_{nc}^{(2)}(k_m,l_R)$. In step 3, the noise- and motion-corrected $g_{nc\&mc}^{(2)}(x)$ is found as $g_{nc\&mc}^{(2)}(x) = g_{nc}^{(2)}(k_m,l=0)$, since the values in the first column corresponds to the decorrelation induced by coagulation only.

Since the method uses the decorrelation to quantify the motion, it can also correct for out-of-plane motion. The lookup table in Fig. 4.2 was created by simulating a noiseless OCT signal exhibiting speckle obtained by randomly moving scatterers —mimicking the coagulation process— along the l index, and uniformly moving scatterers —mimicking bulk motion— along the k index, based on the model of a static sample described by Zaitsev et al. [41]. The method is detailed in Sec. 4.7. The advantage of simulated speckle is that the motion can be accurately modeled and a considerable quantity of speckle patterns can be simulated, allowing for larger ensembles and thus a more accurate calculation of the correlation.

4.3 Materials and methods

4.3.1 Experimental setup

We used a commercial OCT system based on a MEMS-VCSEL wavelength-swept laser at 1310 nm (Thorlabs SL1310V1, Newton, USA) with its imaging module (Thorlabs OCS1310V1, Newton, USA) using a single detector (no polarization-diverse detection) for imaging. We used an Alazar PCI digitizer model ATS9350 to acquire the electronic signal from the imaging module. The laser, with a wavelength range of >100 nm (at -20 dB), has a 16 μm theoretical axial resolution —we determined a 20 μm axial resolution in air experimentally— with an A-line rate of 100 kHz. A CW 532 nm laser (Verdi 10W, Santa Clara, USA) was used as the therapy laser source. A double-clad fiber coupler (DCFC) (Castor Optics DC1300LQ1, Montreal, Canada) was used to couple the therapy laser into the OCT sample arm, which used a single 2.18 m-long double-clad fiber (DCF). The DCF core diameter, cladding diameter, and effective refractive index are all chosen as to match the guided mode waist in SMF-28 fiber and allowed the two fibers to be directly spliced with minimum loss. As shown in Fig. 4.3, OCT illumination and collection are both carried out through the single-mode

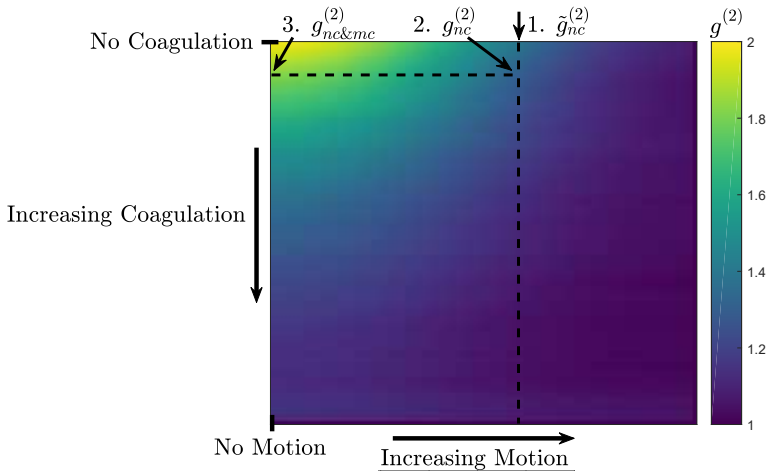


Figure 4.2 Lookup table used for motion correction created from the simulation of coagulation- and motion-induced decorrelation. The vertical axis represents coagulation-induced decorrelation while the horizontal axis represents motion-induced decorrelation. The correction method is as follows: $\tilde{g}^{(2)}_{nc}$ is calculated in an untreated region of the tissue to quantify motion. In step 1. we search for $\tilde{g}^{(2)}_{nc}$ in the first row of the table to determine the motion column index. In step 2. we find the $g^{(2)}_{nc}(x)$ to be corrected for motion in that column and finding its row index. In step 3. we find the $g^{(2)}_{nc\&mc}(x)$ that corresponds to the first value in that row.

(SM) core of the DCF. Meanwhile, the therapy laser is injected into the multimode (MM) end of the DCFC. The use of a single fiber greatly simplifies a future implementation in endoscopy and guarantees co-registration of the two modalities. Furthermore, an extra 1 m of SMF-28 fiber was spliced between the OCT system and the DCFC in order to reduce the ghost artifact described by Beaudette et al. [35] induced by the DCF. For the imaging head, in order to avoid damage due to the high power of the therapy laser and to maintain an achromatic behavior across the therapy and imaging lasers wavelength range, a 7 mm focal length reflective collimator (Thorlabs RC02APC-F01) was used with an UV-enhanced aluminum mirror. The collimated beam had a diameter of 2 mm before being reflected by the galvanometer (galvo) silver-coated mirror (Thorlabs GVS001) and going through the 20 mm focal length uncoated imaging lens resulting in a theoretical beam waist of 20.8 µm and a working distance of 1.06 mm in air.

The therapy laser wavelength was selected because it corresponds with a peak in the absorption spectrum of hemoglobin and because it has been validated extensively in clinical applications [23, 33]. During therapy guidance, the targeted pathology will generally occupy only a portion of the OCT lateral field of view in order to provide a reference for the boundary between diseased and healthy tissue. In order to be able to selectively treat a portion of

the imaging field with the therapy laser, we designed a shutter system. This was achieved by synchronizing a second galvo —the therapy galvo— to alternate between injecting the therapy laser in and out of the DCFC, as illustrated in Fig. 4.3. When the OCT imaging galvo was over the targeted area, the therapy galvo injected the therapy laser into the DCFC. Once the imaging galvo was no longer over the targeted area, the therapy laser was decoupled from the DCFC and sent into a beam dump by the therapy galvo. This effectively created long pulses of 10 mJ and 3 ms at 100 Hz repetition rate. Because this setup for targeting is on the proximal end of the DCFC, it is fully compatible with endoscopic probes. A shutter was used to stop the therapy laser once the targeted therapy duration or coagulation depth was achieved. This shutter was used, instead of the therapy galvo, because the two galvos were synchronized in our setup and could not be driven independently.

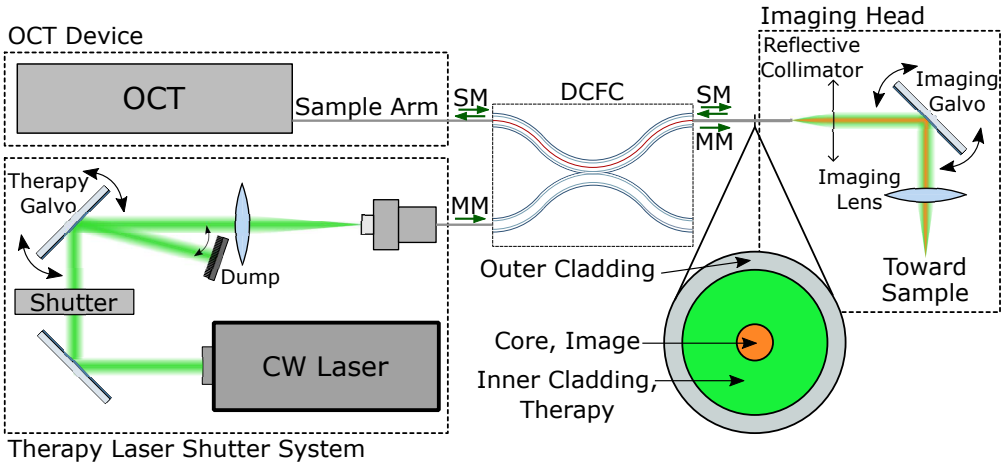


Figure 4.3 Setup used to obtain co-localized imaging and therapy.

In order to test our motion correction, we implemented a setup to emulate patient motion for validation. An electric motor with an unbalanced weight on its rotation axis was used to produce vibrations (see Fig. 4.4). A plastic airbag was used to transfer those vibrations to the sample placed on it. The airbag was wide enough to accommodate 25 cm by 15 cm samples. The frequency of the vibration could be adjusted by changing the motor frequency, and the amplitude by changing the mass of the attached weight. The vibrations reached an amplitude of around 0.3 mm at a rate able to fully decorrelate the speckle at $g^{(2)}(\tau = 10\text{ ms})$.

4.3.2 Software

A custom LabVIEW (National Instruments) application was developed to control both the commercial OCT system, the imaging galvo, the therapy laser galvo synchronization, and

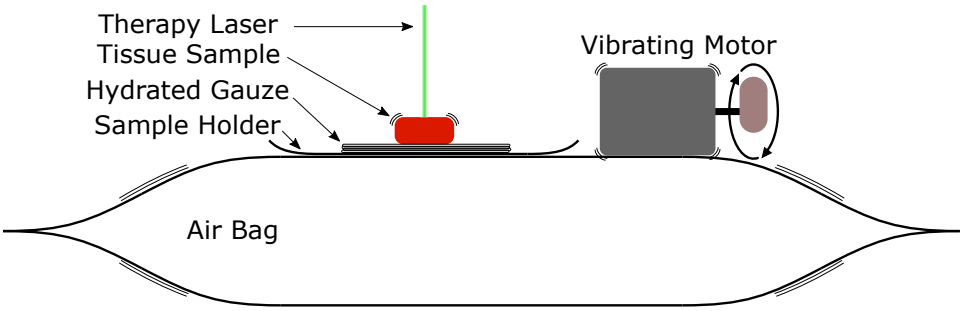


Figure 4.4 Setup used to hold and vibrate sample during experiments.

the laser shutter. The software permits three distinct modes summarized in Table 4.1 and described below.

In order to study the impact of coagulation, noise, and motion on $g^{(2)}$, as well as to validate our model for motion correction, the decorrelation for very small values of τ was calculated. This was accomplished with the first mode called Fast mode. The imaging galvo was set to run at a 1 kHz frequency and a small scanning range while the therapy laser was left to fire continuously. The ensemble size used for calculating $g^{(2)}$ were $\Delta z = 10$, $\Delta x = 16$, $\Delta t = 100$ in pixels or $\Delta z = 77.9\ \mu m$, $\Delta x = 237\ \mu m$, $\Delta t = 100\ ms$ in physical units.

In order to find the appropriate parameters for real-time monitoring and to study the validity of our approach, a second mode, called the Retrospective Diagnostic mode, was developed. It was used to develop our algorithms by recording raw data, allowing us to test our approach with different $g^{(2)}$ parameters. The Retrospective Diagnostic mode showcases how the $g^{(2)}$ can be used to add visual feedback from the therapy by providing real-time structural imaging and recording of the data for retrospective processing with the added control over the therapy laser. A shutter system allowed us to control the therapy laser exposure on the sample. Post-processing calculation of $g^{(2)}$ was performed with an ensemble size of ($\Delta z = 3$, $\Delta x = 10$, $\Delta t = 100$) in pixels or ($\Delta z = 32.5\ \mu m$, $\Delta x = 46.9\ \mu m$, $\Delta t = 100\ ms$) in physical units.

The last mode, called Depth Targeting mode, consisted in the real-time monitoring of the therapy. A region of the tissue not affected by the therapy laser is manually selected to serve as a reference to quantify the bulk motion of the tissue and apply motion correction. An ensemble of pixels is manually selected at the targeted depth and used to check if the depth has been reached in that region. By calculating $g^{(2)}$ in selected regions, computation in real time becomes possible. For a field of view of 2.34 mm (300 pixels) in depth and of 25 mm (800 pixels) laterally, the ensemble size used was ($\Delta z = 3$, $\Delta x = 50$, $\Delta t = 10$) in pixels or ($\Delta z = 32.5\ \mu m$, $\Delta x = 234.4\ \mu m$, $\Delta t = 100\ ms$) in physical units in air. The ensemble size was chosen to have a high resolution in z and t while keeping a good estimation of $g^{(2)}$ in

order to have more accurate automatic coagulation depth determination. It was observed that this larger ensemble size allowed for a more accurate motion correction. Since our goal was coagulation depth with no need to control the lateral extent of the coagulation, a larger size in x was used to allow us to have a finer resolution in z.

Table 4.1 Characteristics of the three system modes

	Fast Mode	Retrospective Diagnostic Mode	Depth Targeting Mode
B-scan Frequency	$\leq$ 1 kHz	$\leq$ 100 Hz	$\leq$ 100 Hz
B-scan Width	$\leq$ 0.35 mm	$\leq$ 25.0 mm	$\leq$ 25.0 mm
B-scan shape	Triangular wave	Sawtooth wave	Sawtooth wave
Max Laser Power	CW: 1.66 W	10 mJ at 100 Hz 3 ms pulse width	10 mJ at 100 Hz 3 ms pulse width
Laser Shutter	Triggered by timer	Triggered by timer	Triggered when targeted coagulation depth reached
Saved Data	OCT fringe data	OCT fringe data	OCT intensity
Typical Δz	10 px or 77.9 μm	3 px or 32.5 μm	3 px or 32.5 μm
Typical Δx	16 px or 237 μm	10 px or 46.9 μm	50 px or 234.4 μm
Typical Δt	100 px or 100 ms	10 px or 100 ms	10 px or 100 ms

To perform real-time motion correction, two reference ensembles on both sides of the treated area were used to calculate $g^{(2)}_{nc}$, using the method described in Sec. 4.2.3. The two ensembles are concatenated into one to calculate a $g^{(2)}_{nc}ref$ value over a larger ensemble, and improve the accuracy of the motion estimation. The ensemble size were $\Delta z = 150$, $\Delta x = 100$, $\Delta t = 10$. We established whether the targeted coagulation depth was reached by testing for two conditions:

$$\begin{aligned} C_1: \ &\textbf{if} \quad g^{(2)}_{nc\&mc}(\tilde{t}) < \xi_1 \text{ for any } \tilde{t} < t. \\ C_2: \ &\textbf{if} \quad g^{(2)}_{nc\&mc}(t) > \xi_2 \ \textbf{and if } C_1 \text{ is satisfied,} \end{aligned} \tag{4.17}$$

where t is the current time index at which the conditions are checked, $\tilde{t}$ is any time index before the current one and ξ_1 and ξ_2 are two threshold values. C_1 consists of checking if the selected region has started to coagulate. As the tissue begins to coagulate, $g^{(2)}$ drops. We can therefore set a certain threshold (C_1) indicative of the start of the process. As coagulation nears completion, $g^{(2)}$ will then return to 2 as the tissue becomes static/stable again. C_2 is set as the threshold indicating the completion of the coagulation process. The values of ξ_1 and ξ_2 were both determined experimentally, as explained in Sec. 4.4.2. The system was capable of verifying both conditions at a faster rate than the B-scan frequency. The data process in summarized in Fig. 4.5. The SNR was estimated using the R versus signal intensity

curve shown in Fig. 4.6. When $\tilde{g}_{nc}^{(2)} < 1.3$ (that is, motion produced a strong decorrelation of the signal), the conditions $\{C_1, C_2\}$ are not computed until $\tilde{g}_{nc}^{(2)} \geq 1.3$. This allowed us to perform coagulation depth tracking despite sudden large motion.

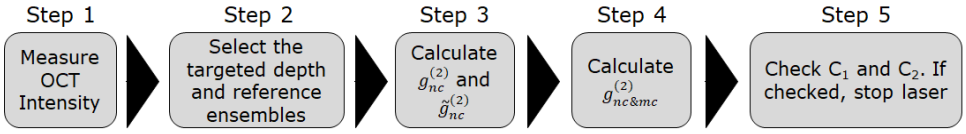


Figure 4.5 Data process steps for real-time monitoring.

4.3.3 Histology

The rat tongue and abdominal muscle samples were taken from a rat a few hours post mortem. The samples were enveloped in a hydrated gauze with Hank's Balanced Salt Solution (HBSS) during transport and kept on an hydrated gauze during the experiment, as shown by the Fig. 4.4. We didn't soak the sample in HBSS in order to avoid the blood in the tissue to diffuse in the solution. Since we are targeting hemoglobin absorption, it is essential to preserve the blood content of the sample.

Once the experiment was finished, the optimum cutting temperature compound was used for frozen section histological processing. The sample was then stored on dry ice until being brought for processing. Hematoxylin and eosin (HE) histology with nitroblue tetrazolium chloride (NBTC) stains for the activity of nicotinamide adenine dinucleotide diaphorase (NADH-diaphorase) were used on slices 10 μm thick in a fashion similar to [12, 82].

4.4 Results

4.4.1 Noise and motion correction

In a first step, we estimated the SNR calibration curve by calculating $g_{nc}^{(2)}$ in 44 B-scans acquired while imaging rat muscle tissue before the start of the therapy. The expected, relatively linear relationship between R_j and I_j is presented in Fig. 4.6. Given Eq. (4.13) predicts a linear proportionality between the SNR and I, a simpler calibration which simply finds $\langle N \rangle$ could work equally well.

The estimation fails at very low SNR values as most of the input is noise. As for other SNR levels, the difference can be explained as well. First, the limited size of ensembles, which adds some uncertainty to the calculated values. Second, the assumption that the noise floor

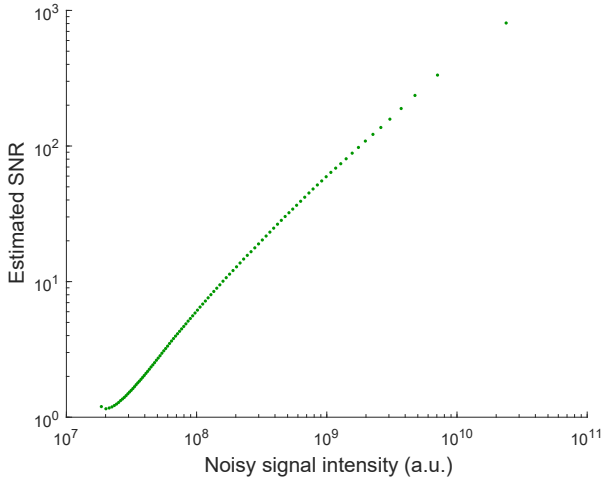


Figure 4.6 Estimated SNR vs. noise intensity calibration curve.

is constant and independent of z, x or t. Third, in an hypothetical incoherent cross-sectional image —that is in absence of speckle— the sample reflectivity will not be completely uniform inside the area corresponding to a single ensemble due to the heterogeneous tissue structure. This implies that assigning a single average intensity to an ensemble is an approximation. Finally, estimating the SNR on very bright spots is limited by saturation of the signal. Despite these limitations, the SNR estimation follows the predicted shape in Eq. 4.15 and allowed us to correct for noise as shown in Fig. 4.7.

The next step was to measure $g_{nc}^{(2)}$ as a function of τ, with the Fast mode described in Sec. 4.3.2, to determine the optimal value for monitoring the coagulation process. Eq. (4.14) was used with a fixed value of z, x and t. This corresponds to using the auto-correlation function to study a static process, because we will limit the analysis to time intervals in which the sample can be assumed to be in a single state (static, coagulating or after coagulation).

In order to observe the effect of the noise correction, the coagulation was performed on an excised sample of rat muscle containing enough hemoglobin to absorb light from the therapy laser. Imaging was performed at a 1 kHz B-scan rate, providing us with a resolution of 1 ms for τ —the shortest decorrelation measurable— and a resolution of 100 ms for t considering the ensemble size Δt —the time scale over which the tissue is assumed to be in the same state— over a width of 0.35 mm, while the therapy laser was left continuously on with an average power of 1.0 W at the sample. The $g^{(2)}$ was calculated at two different depths (z values), for different SNR levels, $R = 8.91$ and $R = 39.03$, with a fixed t for each z during which the tissue was undergoing coagulation at that depth. Figure 4.7 shows how noise correction impacts the calculated $g^{(2)}$ for two different SNR values. As one would expect,

the correction has a more significant impact for lower SNR values. The difference is also more pronounced at shorter delays τ (or higher $g^{(2)}$ values). Implementing noise correction will thus allow for speckle correlation measurements deeper within the tissue, as the OCT SNR dramatically diminishes with depth and coagulation state. The drop of $g^{(2)}$ between $\tau = 0$ and $\tau = 1$ ms is well-known and explained by the noise pattern becoming decorrelated between B-scans, which is not the case for $\tau = 0$, since we are correlating the same noise pattern.

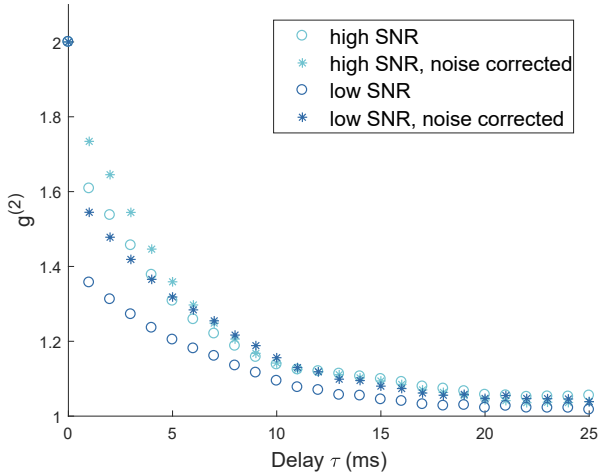


Figure 4.7 $g^{(2)}$ before (circle) and after (asterisk) noise correction for low SNR, $R = 9.50dB$, (dark blue) and high SNR, $R = 15.91dB$, (light blue) values. Color palette from [2].

In our next step, we first validated our simulation model by comparing the total correlation for a range of coagulation-induced and motion-induced decorrelation values for both simulated and experimental data. The process to create the simulated data is described in Sec. 4.7. For the experimental data, we measured the coagulation of rat muscle at 1 kHz with 1.0 W therapy laser power, with a τ resolution of 1 ms. Figure 4.8(a) corresponds to this comparison; the horizontal axis shows the value of $g^{(2)}$ for a range of coagulation-induced decorrelation, while the vertical axis shows the combined effect of coagulation- and motion-induced decorrelation. The dashed lines with unity slope represent simulated and experimental $g^{(2)}$ with no motion, which overlap in Fig. 4.8(a). Motion-induced decorrelation was added by digitally shifting the second correlated ensemble by 1 pixel (7.8 μm) to both the simulated and experimental data (solid lines). The $g^{(2)}$ value drops very similarly in both cases. This validated our approach to create the lookup table for motion correction, which was based on simulated data with digitally added motion. We note that the simulated data was noise free and that the experimental data was corrected for noise.

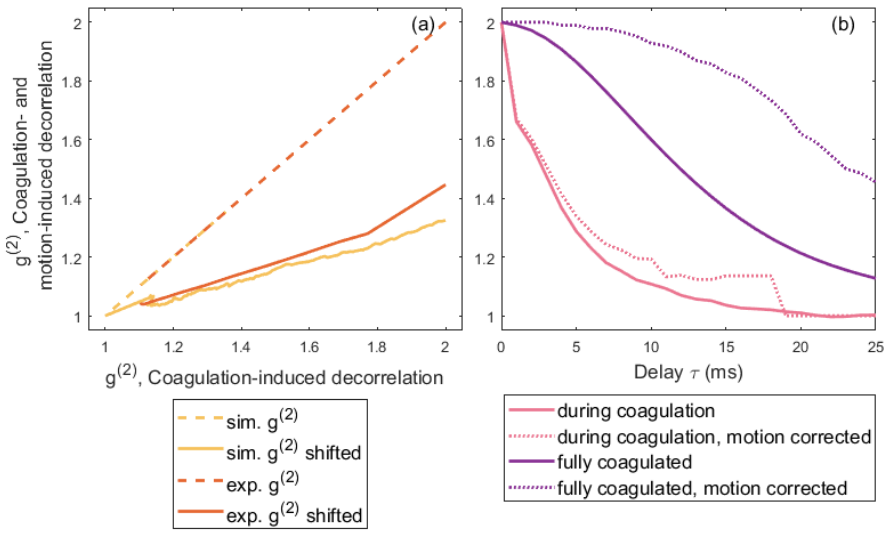


Figure 4.8 (a) Validation of the simulation and motion emulation. $g^{(2)}$ of speckle for simulated (yellow) and experimental (orange) tissue coagulation. Dashed lines represent the data without added motion, both lines are overlapping. Solid lines show $g^{(2)}$ with motion-induced decorrelation added to the coagulation-induced decorrelation. Motion was induced by digitally shifting one of the ensembles by 1 pixel. The figure confirms that motion-induced decorrelation affect simulated and experimental coagulation-induced decorrelation in the same way. (b) Experimental results of the motion correction procedure. $g^{(2)}$ during coagulation (pink curves) and after full coagulation (purple curves), with (dashed curves) and without (solid curves) motion correction. Color palette from [2].

Next, the effect of motion correction on experimental data was evaluated. The OCT scan rate was set at 1 kHz over a small field of view and the therapy laser power was set to 1.0 W. Motion was induced with a motor, as described in Sec. 4.3. $g^{(2)}$ was computed for a fixed z and x for two fixed t corresponding to during and after coagulation with the laser still on in both instances. Coagulation was assessed visually after laser exposure.

In this fast mode, there is no untreated region of the sample that can be used for determining $\tilde{g}_{nc}^{(2)}$ during the treatment. Instead, we assumed that the magnitude of the motion would remain approximately constant during the entire experiment. We thus estimated the motion by determining $\tilde{g}_{nc}^{(2)}$ before the therapy started, and used this same value for all subsequent motion correction. The motion was estimated to range from 6.4 to 6.8 μm per 10 ms. Results are shown in Fig. 4.8(b).

Similarly to the noise correction, motion correction makes the most difference for speckle that should be correlated without motion. Thus, the correction allows us to confirm whether a speckle pattern is stable in the presence of motion. Figure 4.8 also shows the correlation

of the speckle pattern during and after coagulation. As expected, the $g^{(2)}(\tau)$ value decreases much faster during coagulation than after.

4.4.2 Distinguishing coagulated from coagulating tissues

As we see with Fig. 4.8 (b), coagulated tissue can be distinguished from tissue still undergoing coagulation. In this section, we study the variation in time of $g^{(2)}$, for a different tau values. This allows the identification of the optimal tau value, for which the contrast between coagulating and fully-coagulated tissue is maximized. With this in mind, we monitored the coagulation of abdominal rat muscle exposed to 10 mJ pulses at 100 Hz —which is the nominal setting in our system for simultaneous targeted therapy and monitoring— during 3 s. With our system in Retrospective Diagnostic mode (described in Sec. 4.3.2), the therapy laser was put in pulsed mode as to fire only at the center of the OCT field of view with a pulse energy of 10 mJ at 100 Hz, i.e. using 1.0 W of average power.

Figure 4.9 shows the dynamic $g^{(2)}$ as a function of time t during the exposure of the sample to the therapy laser for four different values of τ. $g^{(2)}$ was calculated for an area at the center of the field of view, close to the surface, where the SNR is the highest and the coagulation was guaranteed to complete. In this case, a pixel size ensemble of $z = 3$, $x = 50$, and $t = 10$ was used for a more accurate estimation of $g^{(2)}$ and since high spatial resolution was not a concern. The coagulation spot was visible at the end of the therapy, confirming that tissue did indeed coagulate. From left to right, vertical dashed lines represent moments when the laser was turned on, when tissue motion due to thermal expansion stops (evaluated visually), and when coagulation is reached. For all τ values, a drop in the $g^{(2)}$ value is observed shortly after the laser is turned on. There is often a sudden thermal expansion of the tissue during the initial phase of the coagulation. The expansion is easily identifiable visually. We can see the end of this expansion at the second line when $g^{(2)}$ increases slightly for all values. Finally, at the third line, we can see an increase in $g^{(2)}$ for all values of τ. We estimate the tissue to have finished coagulating at this moment. These results were used in determining our choice of threshold values and τ for the real-time monitoring, which were set from inspection of Fig. 4.9 to $\tau = 10$ ms, $\xi_1 = 1.4$ and $\xi_2 = 1.9$.

The use of threshold values is, however, not necessary to visualize the progression of the thermal coagulation area of the tissue. Figure 4.10 shows a superposition of the decorrelation map over the OCT image for the same experiment. Ensemble size was returned to ($z = 3$, $x = 10$, $t = 10$), since spatial resolution was necessary to know which part of the tissue was affected by coagulation. From left to right, Fig. 4.10 shows the OCT intensity tomogram (a), the $g^{(2)}$ map without (b) and with (c) noise correction and the $g^{(2)}$ overlay in color over

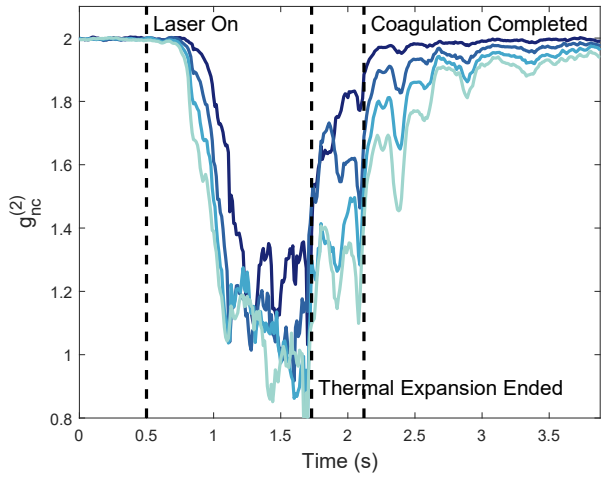


Figure 4.9 $g^{(2)}$ for τ ranging from 10 ms to 40 ms (from dark to pale blue) during laser exposure. From left to right, vertical dashed lines indicate when the laser is turned on, the end of thermal expansion, and when we estimate coagulation to be complete. Color palette from [2]

the OCT tomogram (d). The overlay preserves the structural information from OCT while highlighting the progression of the coagulation. Since Labview does not permit creating the overlay, it was performed in retrospective processing. The refractive index of rat muscle was assumed to be $n = 1.39$ for adjusting the scale of the z axis [83,84]. Coagulation can be seen as the transition from correlated speckle to decorrelated and back to correlated. Coagulated tissue is thus visible as a correlated area in yellow over a decorrelated arc in blue. The progression of the thermal coagulation can also be observed in Fig. 4.11 and Visualization 1. Coagulation was not highlighted with Eq. 4.17 since we found the threshold method to not be reliable with limited ensemble sizes.

Figure 4.11 shows a sequence of OCT images during the therapy of the sample at different time points. The periodic horizontal lines in the intensity are a product of birefringence of muscle at baseline —which is affected by the coagulation process— and the absence of a polarization-diverse receiver in the OCT system.

The final experiment in Retrospective Diagnostic mode consisted of the coagulation monitoring of a moving sample and confirming our result though histology. The parameters used were the same, 10 mJ pulses at 100 Hz, however duration was 5 seconds instead, to adjust for the different optical and thermal properties of the sample. B-scan rate was the same 100 Hz and a $\tau = 10$ ms was used to calculate $g^{(2)}$. Motion was introduced using a vibrating motor and quantified using ensembles on both sides of the targeted area as explained

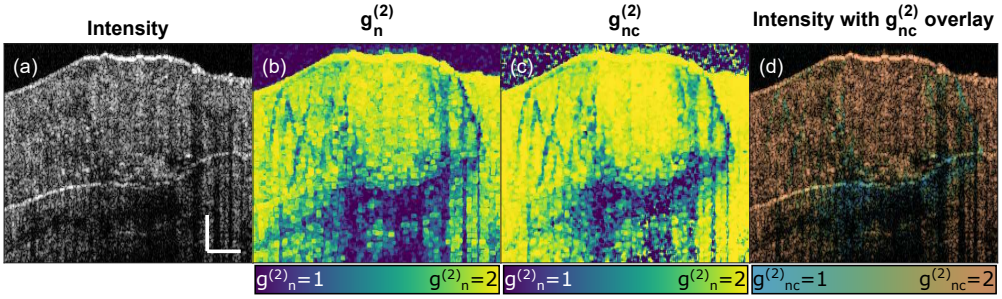


Figure 4.10 Processing steps during Retrospective Diagnostic mode. (a) OCT structural image during therapy, (b) corresponding $g_n^{(2)}$, (c) corresponding $g_{nc}^{(2)}$, and (d) overlay of the OCT intensity (encoded in the luminance) and $g_{nc}^{(2)}$ encoded in the hue of a perceptually uniform isoluminant color map [3]. Scale bars are 0.5 mm.

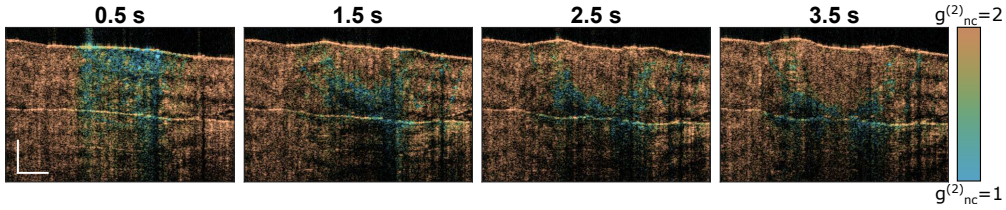


Figure 4.11 Progression of the coagulation highlighted by the correlation of the speckle pattern after 0.5, 1.5, 2.5 and 3.5 seconds of exposure by 10 mJ pulses therapy laser at 100 Hz. Scale bars are 0.5 mm.

in Sec. 3.2. Figure 4.12 shows the coagulation monitoring of the tongue of a rat subjected to motion before (a) and after (b) motion correction, as well as the corresponding histology section (c). The OCT intensity image is shown in (d), which does not exhibit any clear indication of the coagulation depth. Images shown were acquired post laser exposure since we observed that the coagulation continues for a few tens of milliseconds after the laser is turned off. Despite the expected change in shape of the tissue after histological processing —particularly the fold of the tongue which became more pronounced— the coagulation depth observed in OCT matches fairly well that measured with histology. Motion correction improves the visibility of the correlated area corresponding to fully coagulated tissue. More importantly, noise- and motion-correction together are essential in the use of threshold values —described in Eq. (4.17)— for the real-time monitoring of the coagulation depth and automatic interruption of the therapy laser presented in the next section.

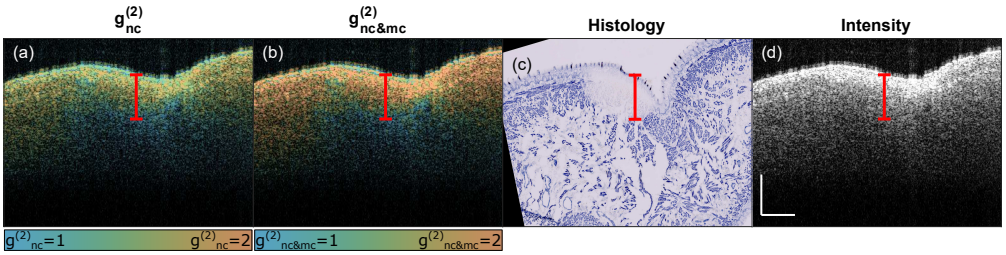


Figure 4.12 Highlighted coagulation of a rat tongue in the presence of vibration (a) without motion correction and (b) with motion correction compared to (c) the histology section. Red markers of identical lengths are placed on each image to facilitate comparison. Scale bars are 0.5 mm.

4.4.3 Monitoring in real-time

The previous images were all created in post-processing with the Retrospective Diagnostic mode. Although images shown in this section were created in post-processing as well, the Depth Targeting mode was used for which a desired coagulation depth is defined interactively on the initial structural image. The correlation is calculated at this targeted depth in real time to perform the coagulation-threshold values checks, outlined Eq. 4.17.

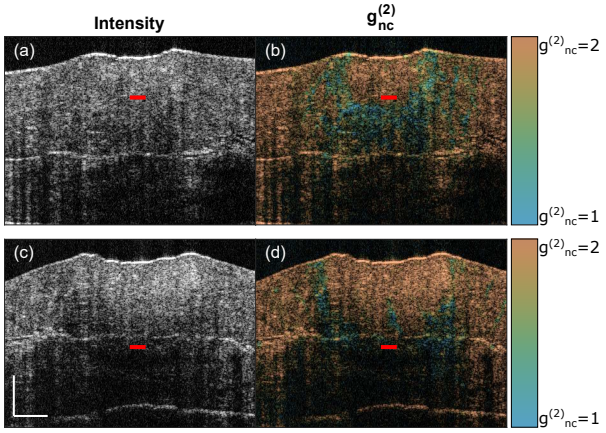


Figure 4.13 Comparison of varying targeted coagulation depths and motion. The coagulation is highlighted by decorrelation map in color while the red bar shows the depth that was targeted. Scale bars are 0.5mm.

We were able to detect the moment the coagulation reached the desired depth and shut the laser off. The experimental parameters are detailed in Table 4.1. Figure 4.13 shows the results from two real-time experiments which were performed targeting two different depths. The overlays correspond to the state of the tissue a few tens of milliseconds after the laser was turned off since the coagulation process continues after exposure. We can see that in the

case of the shallower targeted depth, we seemed to have coagulated deeper than intended. This might be due to the coagulation continuing after the therapy laser closed. In a future implementation, the increase in coagulation depth after the laser is off can be determined experimentally, and the laser can be shut off before in order to reach the targeted depth once coagulation ceases. The difference was not large for the deeper target depth since we observed that the post laser shut off coagulation slows down deeper in tissue.

We performed a final experiment in the presence of induced motion using the technique described previously, with the corresponding results in Fig. 4.14. We targeted a specific depth and compared the real-time estimation of coagulation depth from our technique with histology. The overlays show the tissue tens of milliseconds after the laser was turned off. The OCT overlays shown correspond to only noise-corrected decorrelation and noise- and motion-corrected. The targeted depth, marked by a red line, corresponds well to the coagulation depth determined in the histology. The full video of the results of this experiment are presented in Visualization 2.

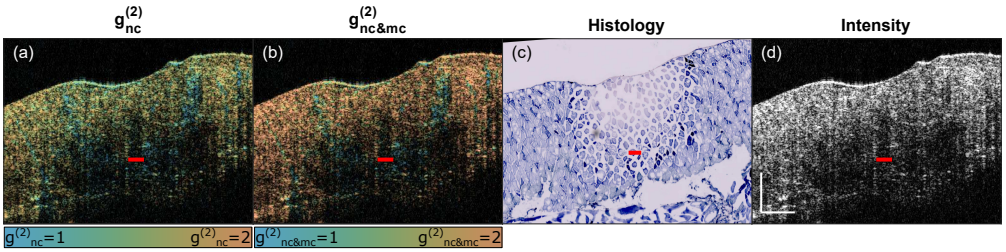


Figure 4.14 Highlighted coagulation during laser therapy was automatically stopped when the targeted depth was reached with histology comparison and OCT tomogram for comparison. The red bar shows the targeted depth. Scale bars are 0.5 mm.

We quantified the motion by obtaining the vertical displacement required to get the drop in decorrelation observed in $\tilde{g}^{(2)}_{nc}$ from the lookup table. We estimate that the decorrelation induced by the motion corresponds to a 55 μm displacement in the axial direction or 108 μm in the lateral direction over 10 ms.

4.5 Discussion

With our laser therapy and OCT system, we demonstrated how the normalized second-order autocorrelation function $g^{(2)}_n$ of the OCT intensity signal could be used to monitor thermal coagulation depth. Noise correction on $g^{(2)}$ gives our system an increased monitoring depth while motion correction makes it more robust to bulk tissue motion. Furthermore, we showed that it was possible to verify whether the coagulation had reached the targeted depth in real

time. Our results were confirmed on an *ex-vivo* sample (rat muscle) through NBTC histology. Since monitoring is based on the signal intensity decorrelation, it does not require the phase signal to be stable. In particular, the compute-intensive phase stabilization and complex-amplitude tomogram interpolation required to correct for non-uniform rotation distortion in endoscopic systems [13] is not required, and instead a simpler intensity-based approach would be sufficient [47]. Combined with the use of a single DCF coupled to a DCFC, the implementation of this approach into clinical catheter systems is greatly simplified.

The coagulation progression was monitored in two ways: one aimed at visualizing the tissue region under active coagulation and letting the operator interpret the corresponding treatment depth (Retrospective Diagnostic mode); the other aimed at automatically determining the treatment depth for automatic laser shut down once the target depth is reached (Depth Targeting mode).

The Retrospective Diagnostic mode was implemented in retrospective processing for our experiments, however it was designed for and is fully compatible with a real-time implementation. Visual feedback is provided by means of overlaying the hue-encoded speckle decorrelation value and the luminance-encoded OCT structural image, preserving the structural information while adding coagulation contrast during the treatment. The progression of the coagulation is readily seen by the transition from a decorrelated state, when tissue is being heated, to correlated, once it has reached coagulation. In this case, we did not automatically detect the coagulation as proposed in Eq. (4.17). The reason for this was the small ensemble size used, ($z = 3$,$x = 10$,$t = 10$) pixels. We found the threshold method to not to be reliable with limited ensembles. In this case, visual estimation by the operator is straightforward. A neural-network approach could potentially replace the operator making the coagulation depth monitoring more robust in this mode.

For the moment, the Retrospective Diagnostic mode was implemented in post-processing due to LabVIEW not allowing the creation of an overlayed image and its limited $g^{(2)}$ computing rate. We confirmed that our custom LabVIEW program using only CPU computing (no GPU) was capable of calculating $g^{(2)}$ on a 400x800 pixels frame using ensembles comprising 10 B-scans at a rate of 5 Hz with both noise and motion corrections. We expect that the use of faster programming language and the implementation of GPU-computing would easily allow our method to run in real-time.

The depth targeting mode was performed in real time, automatically shutting off the therapy laser when the coagulation had reached the targeted depth. We reduced the computation and display demands by calculating the decorrelation for a single ensemble situated at the target. To increase the reliability of the shutting off of the laser, we used a larger ensemble

($z = 3$,$x = 50$,$t = 10$).

Despite high success, in some rare cases a sudden thermal expansion of tissue caused a false positive in the depth detection. The thermal expansion resulted in motion of the untreated, deeper part of the tissue, causing a drop in $g^{(2)}$ followed by an increase —after expansion stops— and thus detected as complete coagulation at a depth not yet reached by the treatment. This phenomenon, easily identifiable visually, caused the automatic stop to trigger, ending the therapy prematurely could be automatically detected by calculating the cross-correlation of the OCT signal in depth to detect large-scale axial motion of the tissue and disable momentarily the coagulation detection. Another limitation of the depth targeting mode is that there is a minimum depth at which we can stop the coagulation, roughly 100 μm in rat muscle tissue. This is due to the laser power spread in depth which causes a coagulation front of finite depth.

In terms of the calculation of the correlation, we observed that the initial noise calibration of the system remained accurate despite changes in the tissue scattering properties, implying that the noise floor of the system is indeed constant throughout the therapy. Thanks to the noise correction, the monitoring depth was limited by the power of our therapy laser and not by the monitoring technique. With a different therapy approach able to deposit energy deeper in tissue the monitoring depth could become limited by the OCT signal attenuation.

Regarding our motion correction, we found it was essential for the depth targeting mode. An obvious limitation of the method arises when the motion causes the speckle pattern to become fully decorrelated, as there is no correction possible to recover the value of the correlation in absence of motion. To mitigate this, we limited the correction of motion-induced decorrelation to $g^{(2)} > 1.3$; for $g^{(2)} \leq 1.3$ we consider any measure of $g^{(2)}$ to be inaccurate and the checking of the coagulation conditions of Eq. (4.17) are not performed. This allows the mode to continue working despite sudden and large motion. Furthermore, a warning message is displayed when this occurs. For our system configuration, this corresponded to approximately 109 μm of axial displacement or 246 μm of lateral displacement between two B-scans. It is interesting to note that the dependence of speckle size on the system resolution implies that a system with poorer resolution would be capable of correcting for greater displacement, at the expense of the spatial resolution and the contrast between the coagulation front and coagulated tissue.

An important aspect of our approach was the determination of the optimal value of τ to maximize the contrast between the coagulated area and static tissue, as well as the optimal threshold values ξ_1 and ξ_2 for the automatic depth targeting. These values are expected to change depending on the absorption of therapy light, tissue thermal properties and the

therapy laser power, wavelength and mode —CW or pulsed [85]. Therefore, prior testing is required to find the optimal parameters for each application.

Another important consideration is the optimal size for the ensemble used to calculate $g^{(2)}$. As stated in the theory, larger ensembles have the advantage of estimating the correlation with a greater reliability, at the cost of a lower resolution in space and/or time. Furthermore, we found that motion correction necessitates larger ensembles to properly estimate and correct the motion. Our choice of ensemble size provided us with a resolution of ~ 32.5 μm in z and 100 ms in time for the automatic coagulation depth targeting mode.

Improvements to the experimental setup include custom coating to the imaging lens to improve transmission for both the OCT and therapy laser transmission, especially in the context of endoscopic imaging. Our proof of principle relied on a chopped CW laser, which greatly limited the available power. In a next iteration, we envision using a pulsed laser in a wavelength range targeting an absorption peak of water.

Furthermore, the fact that the random movement of scatterers mimic the shape of the autocorrelation function of coagulating tissue opens an alternative avenue for correcting for motion. It is known that diffusive motion, another example of scatterer random motion, is described by an exponential decay of the autocorrelation function, in contrast to the Gaussian shape of bulk motion [86–88]. By calculating $g^{(2)}$ as a function of τ for a given t, it is possible to fit an exponential and a Gaussian function, in similarity with the approach to decouple diffusion- from translation-induced decorrelation in dynamic light scattering, and distinguish coagulation- from motion-induced decorrelation. Preliminary testing [89] shows great potential, but requires more computational power to calculate the autocorrelation function as a function of τ in real time.

4.6 Conclusion

In this work we presented a new laser therapy monitoring technique that allowed us to monitor the progression of thermal coagulation of excised animal tissue. A 532 nm therapy laser was used with OCT imaging through a single double-clad fiber compatible with endoscopic use. The use of a single fiber allows for simultaneous and co-registered imaging and therapy. We present the use of a normalized second-order autocorrelation function to measure the decorrelation of the speckle pattern occurring during coagulation. We implement an analytical noise correction that extends the therapy monitoring depth beyond the penetration depth of the therapy laser. We also implement a numerical motion correction technique that makes our technique robust against bulk tissue motion. Using a threshold scheme, we are able to

detect, in real-time, when the coagulation had reached the targeted depth and automatically turn the therapy laser off. Relying on the dynamics of speckle during coagulation addresses fundamental limitations of techniques that rely on the change of tissue birefringence —which require tissue with birefringence at baseline and a polarization-sensitive OCT system, or the attenuation of the OCT signal —which are known to underestimate the therapy depth. Finally, in contrast with alternative methods that rely on the complex-amplitude signal decorrelation, our monitoring scheme does not require the phase of the OCT signal, further facilitating real-time implementation in endoscopic OCT systems, thanks to the enabling of simplified correction approaches for non-uniform rotation distortion artifacts.

Funding

National Institutes of Health (NIH) (K25 EB024595).
Fonds de recherche du Québec - Nature et Technologies (FRQNT) (2018_PR_208631).

Acknowledgments

The authors would like to acknowledge Édith Ducharme, Xavier Attendu and Martin Poinsinet De Sivry-Houle for useful discussions, and Irene Londoño for histology.

Disclosures

NUP: Terumo Corporation (P), CB: Castor Optics, inc. (I,P).

4.7 Appendix A - Speckle simulation

In this Appendix we present the procedure used to numerically simulate speckle patterns to study the combined effect of motion and thermal coagulation on $g^{(2)}$. We randomly distributed an ensemble of scatterers and simulated light from an illumination beam being reflected off of those scatterers, producing a two-dimensional speckle pattern [41]. Coagulation was simulated by randomly moving the scatterers individually, while bulk tissue motion was added with a sub-pixel displacement. $g^{(2)}$ calculated from the resulting speckle patterns were assembled into the lookup table presented in Fig. 4.2. Simulation parameters are included in Table 4.2.

The first step consisted of simulating the position of randomly distributed and moving scatterers. We start by defining our simulated environment pixels z and x positions, p_{z0} and p_{x0},

as follows:

$$\begin{aligned} p_{z0}(z) &= (z-1)\cdot px \text{ for } z \in \{0,1,2,\ldots,s_z-1\}, \\ p_{x0}(x) &= (x-1)\cdot px \text{ for } x \in \{0,1,2,\ldots,s_x-1\}, \end{aligned} \tag{4.18}$$

where z and x are the pixel indexes, s_z and s_x are the size of the simulated environment and px is the physical size of the pixels, assumed to be the same in z and x for simplicity. We then randomly distributed the scatterers:

$$\begin{aligned} p_{zs}(z,x,n,t=0) &= \epsilon_{1z}(z,x,n)\cdot px + p_{z0}(z), \\ p_{xs}(z,x,n,t=0) &= \epsilon_{1x}(z,x,n)\cdot px + p_{x0}(x), \end{aligned} \tag{4.19}$$

where $p_{zs}(z,x,n,t=0)$ and $p_{xs}(z,x,n,t=0)$ are the physical locations, in the z and x directions respectively, of the n-th scatterer in pixel (z,x). There is thus multiple simulated scatterers per pixel for a total number of s_n scatterers per pixel. ϵ_{1z} and ϵ_{1x} are randomly generated numbers uniformly distributed from 0 to 1. Random motion is then added to simulated tissue coagulation [89]

$$\begin{aligned} p_{zs}(z,x,n,t) &= p_{zs}(z,x,n,t-1) + m_a\cdot\epsilon_{2z}(z,x,n,t), \\ p_{xs}(z,x,n,t) &= p_{xs}(z,x,n,t-1) + m_a\cdot\epsilon_{2x}(z,x,n,t), \end{aligned} \tag{4.20}$$

where $\epsilon_{2z}(z,x,n,t)$ and $\epsilon_{2x}(z,x,n,t)$ also are randomly generated number with a uniform distribution between 0 and 1. The amplitude of the movement is scaled by changing m_a value. We then simulate how OCT light is reflected by our scatterers. We simulated a Gaussian point spread function (PSF) centered on each pixel and summed the resultant electric field reflectivities

$$E(z,x,t) = \sum_{Z=1}^{s_z}\sum_{X=1}^{s_x}\sum_{N=1}^{s_n} \exp\left(\frac{-[z-p_{zs}(Z,X,N,t)]^2 - [x-p_{xs}(Z,X,N,t)]^2}{2w^2}\right) \exp\left(-2i\pi p_{zs}(Z,X,N,t)\right), \tag{4.21}$$

where E is the resulting complex electric field on each pixel and w is the beam waist of the PSF assuming Gaussian illumination. The simulation thus accounted for both the amplitude and phase of the backscattered light. We are, however, interested in the signal intensity:

$$I(z,x,t) = |E|^2. \tag{4.22}$$

The process in Eqs. (4.20) and (4.21) is repeated to obtain a speckle pattern changing in

time in response to the dynamics of the scatterers. The next step consisted of calculating $g^{(2)}$. We defined the ensembles I_1 and I_2 as follows:

$$\begin{aligned} I_1 &\equiv \{I(z,x,t=0)\}, \forall z \text{ and } \forall x \text{ and} \\ I_2(\tau) &\equiv \{I(z,x,t=\tau)\}, \forall z \text{ and } \forall x. \end{aligned} \tag{4.23}$$

The variable τ defines the delay. Since we also wanted to simulate bulk tissue motion, instead ot adding it in Eq. (4.20), we decided to shift $I_2(\tau)$ by a subpixel amount based on previous works on subpixel registration [90–92]:

$$\begin{aligned} Z &= \mathcal{F}(I_2(\tau)), \\ z_{shift} &= \exp(-2i\pi\Delta), \\ Z_{shifted} &= Z \cdot z_{shift}, \\ I_2(\tau,\Delta) &= \mathcal{F}^{-1}(Z_{shifted}), \end{aligned} \tag{4.24}$$

where $\mathcal{F}$ denotes a two-dimensional discrete Fourier transform implemented through a fast Fourier transform algorithm, and $\mathcal{F}^{-1}$ is the corresponding inverse discrete Fourier transform. Δ is the shift value in pixels ranging from 0 to $\Delta_{\max}$. Since we shifted $I_2(\tau,\Delta)$ towards the bottom, the top of the speckle pattern will no longer be spatially correlated. We thus cropped the wrapped regions before calculating g2. I_1 and $I_2(\tau,\Delta)$ become

$$\begin{aligned} I_{1c} &\equiv \{I_1(z,x)\}\, \forall z \in \{\Delta_{\max}+1, \Delta_{\max}+2, \ldots, s_z\} \text{ and } \forall x \text{ and} \\ I_{2c} &\equiv \{I_2(\tau,\Delta)(z,x)\}\, \forall z \in \{\Delta_{\max}+1, \Delta_{\max}+2, \ldots, s_z\} \text{ and } \forall x. \end{aligned} \tag{4.25}$$

We finally calculated $g^{(2)}$ for varying values of τ and Δ

$$g^{(2)}(\tau,\Delta) = g_n^{(2)}(I_{1c}, I_{2c}(\tau,\Delta)), \tag{4.26}$$

where $g_n^{(2)}$ is defined in Eq (4.6). To calculate the decorrelation map, we used the parameters in Table. 4.2.

Table 4.2 Speckle simulation parameters

Variable	Value	Description
p_x	10 μm	pixel physical size
s_z	120	Number of pixels in z direction
s_x	120	Number of pixels in x direction
s_n	10	Number of scatterers per pixel
m_a	0.1 μm	Maximum amplitude of scatterers random movements
τ	0,1,2,...,200 frames	Delay of $g^{(2)}$
Δ	0,0.025,0.05,...,5 pixels	Global movement amplitude
$\Delta_{\max}$	5 pixels	Maximum global movement amplitude
w	4.25 μm	PSF beam waist

CHAPTER 5 ALTERNATIVE METHODS AND OTHER FINDINGS

This section is dedicated to results and discoveries that were made, but were either inconclusive or not developed enough yet to be published in an article. We explore calculating $g^{(2)}$ at different τ to differentiate motion and coagulation-induced decorrelation and using Artificial Intelligence (AI) as an alternative to computing $g^{(2)}$.

5.1 Coagulation-Induced Speckle Decorrelation

5.1.1 Chosen Approach

Most approach for motion correction are either based on 3D C-scan [93, 94], are limited to in-axis motion correction for B-scan measurements [94–96] or necessitate phase stability [46, 97, 98]. We wanted a method capable of correcting both for in and out-axis motion with only B-scan measurements.

Our initial approach to study the effect of motion on coagulation-induced decorrelation was analytical. We tried to calculate the expected values of $g^{(2)}$ by adding a displacement to the PSF similarly to [10]. It was unfortunately unsuccessful and we oriented ourselves toward a simulation to find the relation.

One of the advantages of using a simulation is that we are no longer restricted by the number of pixels in our ensembles when calculating the $g^{(2)}$. We know that the $g^{(2)}$ accuracy of the speckle pattern depends on the number of points used calculating it. Furthermore, in the case of the simulation, we are certain that the decorrelation value is constant across the entire ensemble as opposed to in the experiment case, coagulation may induce more decorrelation in one portion. We can also have a noiseless speckle pattern.

The simulation method is the one detailed in Chapter 4. Tissue coagulation was initially modeled as a random change in position and reflectivity of the different scatterers in the simulation. This, in turn, modifies the amplitude and phase of light being reflected from those scatterers, and, thus, result in the interference changing causing the dynamic speckle pattern. The issue in implementing this approach is that we do not know how position and reflectivity randomly vary during coagulation. We do not know the probability density functions for these random variables describing the changes in position or reflectivity.

To solve this, we consider them to be independent random variables. Since what interests us is the result from the sum of the complex signal reflected, the sum respects the central limit

theorem [40]. Thus, the resulting density function, the sum of those independent random variables, is a Gaussian distribution in the complex plane centered around the speckle value before change.

Note that this is only valid if the change in position and reflectivity is independent from one scatterer to the next. This is not quite the case. As stated before, it has been observed that the scattering coefficient increases when tissues coagulate, indicating a certain correlation in the change of reflectivity. However, the increase in the time scales of interest is very small and was thus neglected. Furthermore, we assumed that the change in the scatterers' position would be randomly independent. Yet, as mentioned, motion in a uniform direction has been observed during coagulation from tissue expansion. [10] We again neglect this since the amplitude of the expansion is rather small and was estimated to not be the main cause of decorrelation.

Moving on, we cannot directly simulate our coagulation by using a random Gaussian density function. This would only be valid for a speckle pattern that is not correlated in space. As explained in Chapter 2, this spatial correlation is due to the PSF of the Optical Coherence Tomography (OCT) beam being wider than the imaged pixels. This is why, instead, we simulated the change on the individual scatterer. A uniform random density function ranging from 0 to a maximum was used to simulate the random changes with the choice of the maximum controlling how fast the resulting speckle pattern would decorrelate. The exact nature of these density function does not matter, because, as explained, the resulting sum will follow a Gaussian distribution.

A similar method to how the scatterers position is changed described in Section 4.7 of Chapter 4 was used to simulate the change in reflectivity. The initial values are described as:

$$r(z, x, n, t = 0) = \epsilon_3, \tag{5.1}$$

where ϵ_3 is randomly generated number with a uniform distribution between 0 and 1. The change is then added:

$$r(z, x, n, t) = r(z, x, n, t - 1) + m_b(\epsilon_4 - 0.5), \tag{5.2}$$

where m_b is the maximum possible change of the reflectivity and ϵ_4 is also randomly generated number with a uniform distribution between 0 and 1. As to make sure that the reflectivity would not go lower than 0 or higher than 1, which would be unrealistic, we added a condition

to avoid it:

$$\begin{aligned} &\textbf{if} \quad r(z,x,n,t) < 0 \text{ then } r(z,x,n,t) = 0 \textbf{ or} \\ &\textbf{if} \quad r(z,x,n,t) > 1 \text{ then } r(z,x,n,t) = 1. \end{aligned} \tag{5.3}$$

Equation 4.21 then becomes:

$$E(z,x,t) = \sum_{Z=1}^{s_z} \sum_{X=1}^{s_x} \sum_{N=1}^{s_n} r(z,x,n,t) \exp\left(\frac{-[z - p_{zs}(Z,X,N,t)]^2 - [x - p_{xs}(Z,X,N,t)]^2}{w^2}\right) \exp\left(-2i\pi p_{zs}(Z,X,N,t)\right), \tag{5.4}$$

The last step consisted in adding a uniform motion to our simulated space. In order to save simulation time, this was done with a subpixel shift of the artificial tomogram. In order to test for very small displacements, instead of increasing the resolution and thus increasing the simulation time, we used the phase shift described in Chapter 4.

5.1.2 Results

Our first test was to compare how the different causes of decorrelation - changes in scatterers reflectivity, position and uniform motion - affect $g^{(2)}$. Three separate simulations were made and the results are shown in Figure 5.1. The same parameters as those in Table 4.2 from Chapter 4 were chosen with the only exceptions being $\Delta = 0.0667\tau$ and $m_b = 0.1$. We immediately notice that both a reflectivity and position change affect $g^{(2)}$ in the shape of an exponential curve. This result is expected since, as described in the previous section, the resulting phasor will follow a normal random distribution no matter what the exact random process governing the changes on the individual scatterer is. This is also the reason we only simulated scatterers motion since simulating reflectivity was redundant. The fact that the two curves exactly overlap like this is, however, a coincidence in the choice of parameters in the simulation.

We see, however, contrary to the other two, the uniform motion in purple follows a more Gaussian curve. Since all scatterers are now moving in the same direction, the random variables are no longer independent and the central limit theorem is no longer valid. The Gaussian shape is most likely a consequence of the PSF shape that is also Gaussian and is responsible for the speckle's spatial correlation. In fact, a uniform motion of the tomogram amounts to calculating the autocorrelation in space instead of time.

To confirm our simulation results, we measured $g^{(2)}$ of coagulating tissue experimentally in Figure 5.2. We used the Fast Mode described in Chapter 4 on beef muscle, but with a therapy

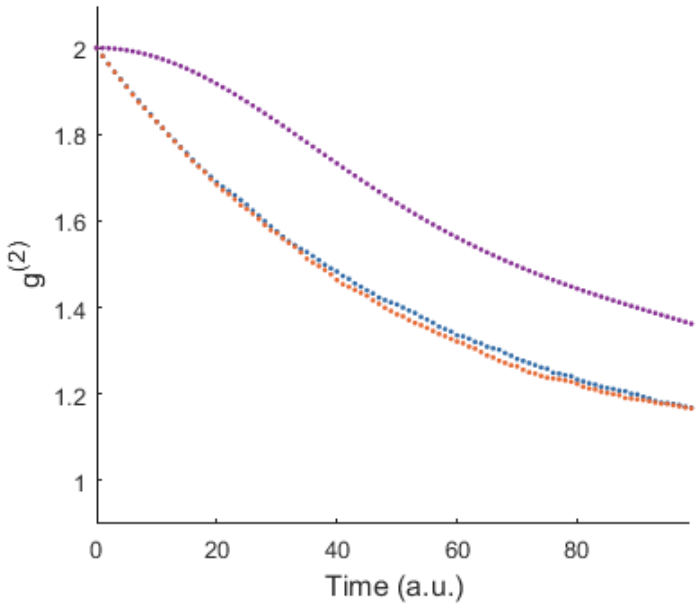


Figure 5.1 $g^{(2)}$ for simulated speckle patterns. The decorrelation was induced by a change in reflectivity, in orange, a change in position, in blue, and a uniform motion of the scatterers, in purple.

laser power of 1 W. Also, the sample was artificially moved digitally as described in the same Chapter. Though the difference is less pronounced, we can still see that the curve of the coagulating muscle has a more exponential shape than the other one. Though not large, a difference between decorrelation induced by motion or coagulation is present.

We thought of exploiting this difference as another means to differentiate motion- and coagulation-induced decorrelation. The idea is to fit a Gaussian and an exponential function on $g^{(2)}$ and quantify the contribution of both as follows:

$$g^{(2)}(\tau) = \exp\left(-(A\tau)^2\right)\exp\left(-B\tau\right) + 1, \tag{5.5}$$

where A and B are the coefficients that we find through the fit. Notice that the fit gives $g^{(2)}(0) = 2$, as we would expect, and $g^{(2)}(\tau \to \infty) = 1$ for $|A| + |B| \neq 0$, meaning speckle should eventually completely decorrelate in the presence of some motion or coagulation. Furthermore, we notice the following relations:

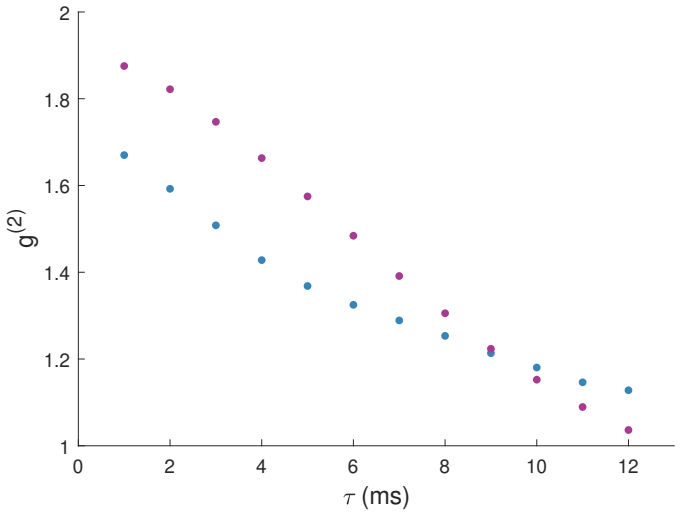


Figure 5.2 $g^{(2)}$ of a moving beef muscle in purple and of it coagulating but not moving in blue.

$$\begin{aligned} \exp\left(-(A\tau)^2\right) &\to 1 \text{ for } A \to 0, \\ \exp\left(-B\tau\right) &\to 1 \text{ for } B \to 0. \end{aligned} \tag{5.6}$$

This means that the closer the coefficient is from 0, the less the corresponding part of the equation, the corresponding source of decorrelation, influences $g^{(2)}$. To test this strategy, we calculated $g^{(2)}$ for the same simulated speckles but with an increasing Δ shift of the speckle pattern. The results are shown in Figure 5.3. We fitted Equation 5.6 on each curve and showed the resulting coefficient in Table 5.1. We notice that A, the coefficient associated with motion, increases with the amplitude of Δ, the induced motion, while B, the coefficient quantifying the coagulation, remains somewhat constant.

Table 5.1 Coefficients A and B for varying motion.

Δ/τ (a.u.)	Variable A	Variable B
0	6.262e-09	0.01772
0.004	0.007616	0.01868
0.008	0.01688	0.01961
0.012	0.02339	0.02217

The next step was to see if we obtained the same result for simulated speckle patterns having the same motion but different coagulation-induced decorrelation. The different coagulation

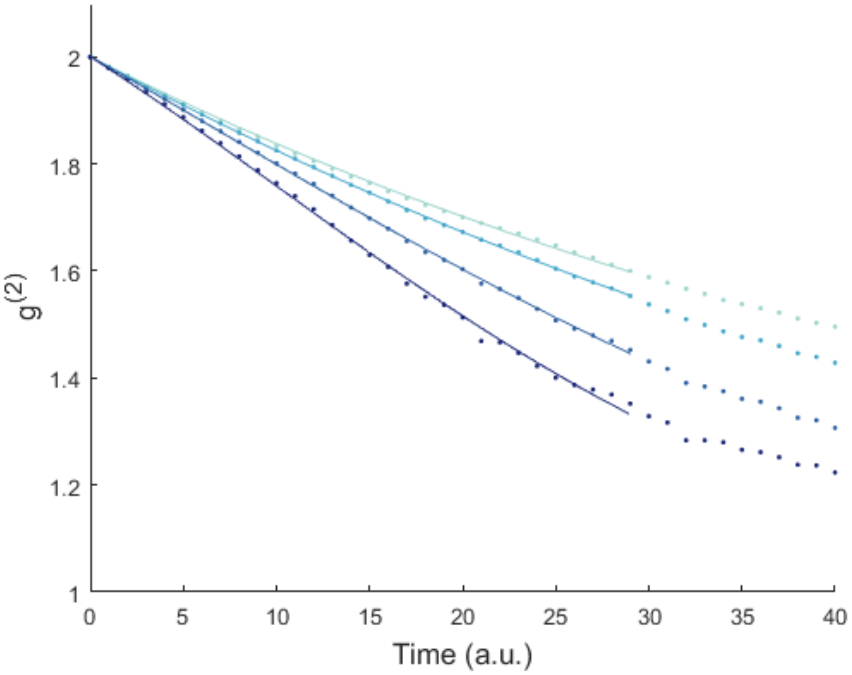


Figure 5.3 $g^{(2)}$ of simulated speckle pattern. The speckle pattern was shifted for different amplitude going from lighter blue, for no shift, to a darker blue, for our maximum shift.

rate was made by changing the time scale for each case. For example, in case one, a $\tau = 1$ was the equivalent of correlating the first B-scan with the second; in case two, $\tau = 1$ was the equivalent of correlating the first B-scan with the third instead; in case three, $\tau = 1$ it was the first with the fourth and so on. In all four cases, the speckle pattern was shifted by the same Δ. The result is shown in Figure 5.4, while the coefficients of the fits are shown in Table 5.2. Similarly to the previous strategy, we notice that A remains somewhat constant, indicating that the motion would be the same, while B increases with the rate of coagulation.

Table 5.2 Coefficients A and B for varying coagulation.

steps Time factor	Variable A	Variable B
1	0.02185	0.01978
2	0.02001	0.03857
3	0.01936	0.05619
4	0.02204	0.07256

These are promising results, but there are still issues in using this method in real applications. First, it is necessary to calculate $g^{(2)}$ for very small τ. This mean that a faster scan rate is essential. As the A-line rate of OCT systems are limited, this means restricting the

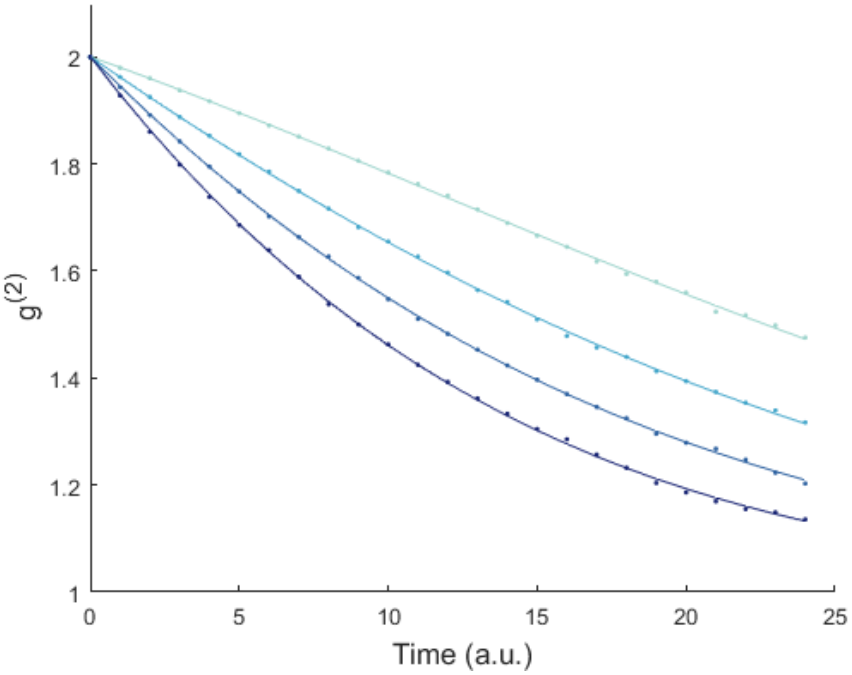


Figure 5.4 $g^{(2)}$ of simulated speckle pattern. The speckle pattern was shifted for the same amplitude, varying coagulation rate. Going from lighter blue, for the slower rate, to a darker blue, for the fastest.

lateral FoV as we did in Chapter 4. Otherwise, it is unknown if making these fits is too computationally heavy to be realized in real time. Finally, we have yet to successfully use this method to quantify the coagulation experimentally. It remains, however, an interesting possibility to explore.

5.2 Neural Network

Artificial Intelligence (AI) was shortly explored as a better alternative to using $g^{(2)}$. Our approach was mainly based on the Matlab Neural Network toolbox and tutorials available on internet. The goal was to train a Neural Network (NN) to track the coagulation progression in the presence of motion and with a low Signal to Noise Ratio (SNR) signal. This section covers our approach, preliminary results as well as obstacles that were encountered.

To train a NN, a great volume of experimental data with corresponding analyzed results are required. This implies making a lot of experiments, which would be doable, and knowing the resulting coagulation depth of all of them, which is problematic. We could use the method described in the article, but in that case, all we would be doing is training our AI to copy

what we have already achieved through this method. It would be pointless. This means that we need to validate the results through another means which would be histology. Given the difficulties of obtaining histology results in such quantity, we decided to train our NN with simulated data instead.

In a first step, the simulation in the previous section was used to train a NN in calculating $g^{(2)}$ of our simulated speckle pattern. This served as an exercise. It was accomplished by using a Matlab Neural Network toolbox with a Feedforward neural network with three hidden layers of 100, 20 and 10 neurons in that order. The choice of layers and neurons were obtained by trial and error since there exist no real answer to the required amount necessary. [99–101] To train it, we simulated two frames of wide speckle patterns, 100x100 pixels, with varying decorrelation intensity to be able to have an accurate calculation of various values of $g^{(2)}$. The NN was fed a reduced version, 10x10 pixels, of the simulated pixels with the previously calculated $g^{(2)}$ result. The fed speckles were smaller since we did not want our AI to rely on a large ensemble. The training manages to converge and our NN was then successfully capable of estimating $g^{(2)}$.

The second step was to add noise and motion. A wide speckle pattern was first simulated without noise or motion and $g^{(2)}$ was calculated as before. The motion was then added using the Fourier shift previously described and noise was added as a white-noise contribution to the complex-valued tomogram as described by Equation 2.7. This time, however, sets of 11 frames were simulated so that our AI could have information on how the speckle decorrelates at various τ. The NN was fed with the reduced, moving and noisy speckle patterns, but the $g^{(2)}$ calculated before the added noise and motion.

Eventually, a conversion of the NN was obtained with three hidden layers of 200, 100 and 10 neurons. We then tried to apply it to real OCT tomograms. It dit not work. At first, we hypothesized that we simply needed to normalize the tomogram signal intensity to be on the saved scale as the simulated data. Unfortunately, the NN continued to give inaccurate $g^{(2)}$ values. Values often lower than 1 or higher than 2, the expected minimum and maximum values for $g^{(2)}$. In the case of experimental speckle patterns, the AI seemed to give random results.

In the end, due to a lack of time and the fact that it was a side project, the issue was never solved and the idea was abandoned. We remained convince, however, of its potential. A better method might have been to, instead of feeding the result as a $g^{(2)}$ value, feed it as a binary coagulated or not value.

CHAPTER 6 GENERAL DISCUSSION

During this project, we studied the possibility of using OCT speckle decorrelation occurring during tissue thermal coagulation to monitor laser therapy. We successfully controlled the coagulation depth of an ex-vivo sample while in the presence of motion. The results were confirmed with NBTC histology. We further explored using multiple values of τ in calculating $g^{(2)}$ as an alternative to the motion correction and using AI to completely replace $g^{(2)}$. Both of those methods have, however, yet to produce accurate experimental results. Here, we will critique our overall methodology.

6.1 Signal Treatment

As mentioned in Chapter 3, a coagulation simulation was created. Though the simulation results were not as useful as anticipated, it did prove to be very formative in understanding the different dynamic between light scattering, absorption and the dissipation of heat in biological tissue. It also played a role in estimating the laser power necessary for our experiment and thus choosing the right tool. It was, however, a bit of an overkill for the part that it played.

Moving on, our main tool in this work to quantify the speckle decorrelation was second-order correlation function ($g^{(2)}$). With it, we were successfully able to monitor the progression of coagulation in real-time, answering our objective. We further developed the method by adding an analytical noise correction, increasing the maximum monitoring depth. A similar approach was attempted for motion correction, but a more experimental method was ultimately chosen. The correction allowed our automatic coagulation depth detection to continue working in the presence of a uniform motion of the sample. What had yet to be accomplished was creating the colored image in real-time. Labview, however, was ill-suited for this. To achieve it, it would have been necessary to explore an alternate programming language and try our hand in GPU computing to accelerate the process.

Furthermore, it would have been more rigorous to directly compare our method to the OCT based ones that were previously developed in the literature to establish the effectiveness of our approach. These include CDV, change in scattering and Doppler based methods. This meant, however, developing entire new analysis algorithms that were not the focus of our work.

During the project, we did make an unexpected discovery in how the shape of the $g^{(2)}$ function was different depending on how the scatterers decorrelate the OCT signal. Motion-

and coagulation-induced decorrelation have two different effects. The difference between the two has to do with the correlation of the movement of the scatterers. In the case of movement, from the point of view of the OCT, all the scatterers move in the same direction. The individual movement of the scatterers are not independent. For the coagulation, the motion of the scatterers, or their change in reflectivity, is at least partially independent from one another, allowing us to approximate them as random independent variables.

Using this method implied calculating $g^{(2)}$ for very short delays τ. This could be challenging to achieve since the minimum possible value of τ is linked to our OCT scanning rate. Even then, there is still work needed to be done before distinguishing the combined effect of the two. Since we would no longer need ${}^{R}g^{(2)}_{nc}$, we could use a CW therapy laser and scan a smaller part of the sample achieving the required scan rate.

A missed opportunity of the project was the study of ablation monitoring. The laser at maximum power used could only just succeed in causing ablation in some cases. The solution for monitoring the depth of ablation would have been a surface detect algorithm and see how the surface in the middle of the scan deepens compared to the surrounding.

Another alternative method studied was the use of artificial intelligence. The technique has gained popularity in diagnostic of illness. A properly trained NN should be able to analyze our data and come to the correct conclusion. In our case, we were able to successfully trained our AI with simulated data, but the obtained NN did not work on experimental OCT data.

6.2 Imaging System

Our imaging system was rather minimal. A galvo mirror with an injection set-up was used to make our CW 532 nm laser pulsed at the same rate as our OCT B-scans. A Double-Clad Fiber Coupler (DCFC) was used to combine the signal of both the OCT and therapy laser in a single Double-Clad Fiber (DCF). The OCT signal was transmitted and collected by the core of the DCF while the inner cladding was used for the therapy laser. The imaging head of the OCT was limited to a reflective collimator followed by a galvo mirror and a uncoated imaging lens.

Though it was enough for our tests, with more time and equipment, it would have been pertinent to try our approach with a catheter endoscope to further validate our approach. Given that catheter system for the esophagus often use either a balloon or capsule, it would have put a pressure on the surface of the tissue being coagulated. We do not know how this would have affected the tissue thermal expansion and thus the monitoring of the therapy. Furthermore, though not necessary for our experiment, a more ideal system would be using

lenses coated for both the therapy and OCT lasers.

Finally, our therapy laser was far from ideal. Though the choice of wavelength seemed like a good idea initially, we later discovered how some ex-vivo samples lose the blood and thus the absorbers targeted by a 532 nm laser. This includes an esophagus which was supposed to be the sample used in our submitted article. Furthermore, our pulsed method was very inefficient. It was the main reason why ablation could not be achieved. Ideally, given the absence of affordable suited laser, we would have made our own. This decision would have needed to be taken at the beginning of the project, however, as making a laser is no simple endeavor.

6.3 Sample

In the end, our project uses ex-vivo rat muscles as samples. For the Nitroblue Tetrazolium Chloride (NBTC) histology to work, it requires freshly sacrificed samples. We had planned to use a porcine esophagus given that one of our main application is for Barrett's esophagus. Since the sample was preserved in Hanks' Balanced Salt Solution (HBSS) combined with a loss of blood pressure after death, the epithelium layer had no blood in it. This meant that our therapy laser could not heat our target. The rat muscle was chosen as an alternative for their accessibility, their rich content in blood even after death and the visibility on the OCT of the different muscle layers that could be used as a reference to judge the coagulation depth.

The difficulties encountered for histology explains their limited amount. Despite using reference papers, it took us a great amount of time before developing a successful protocol. Even then, the coagulation spots were hard to find during the histology cuts and they had a tendency to break down, making the results useless.

CHAPTER 7 CONCLUSION AND RECOMMENDATIONS

7.1 Summary of Works

As stated in the article, thermal coagulation depth control was achieved in ex-vivo rat muscle samples. It was accomplished by using a DCFC to achieve co-registered OCT imaging and laser therapy at the same time. Many difficulties remain to be solved, however, before the system can be introduced to the clinic.

7.2 Signal Treatment

The second-order correlation function was used to provide contrast to coagulated tissues. The technique also has the advantage to allow automatic detection of coagulation depth. The noise correction allows for an extended monitoring maximum depth while the motion correction helps with making the system more robust to motion.

It still has a few shortcomings, however. The two conditions threshold need improvement in order to avoid false positive during tissue expansion. Furthermore, we had difficulties in measuring reliable correlation value due to small ensembles. This limits the resolution of our approach. Combined with our motion correction, this introduced an additional small error; large ensembles are necessary to obtain reliable results.

The reliability of our method still needs to be tested in-vivo to confirm its viability. Only in-vivo measurement will allow to confirm whether motion correction works as intended. In-vivo experiments are also necessary to confirm no unforeseen problems would appear in practical applications. Further research is still necessary for it to become a clinical technique.

7.3 Therapy Laser

A 532 nm CW laser was used to thermally coagulate our samples. An injection system using a galvo mirror with a DCFC was used to have the laser pulsed at a control pulse frequency and width. Though it worked, the system was less than ideal.

The use of the 532 nm wavelength limited us to samples with only hemoglobin present. This was an issue for ex-vivo samples and we recommend targeting water absorption for future ex-vivo research. Furthermore, our system requires a pulsed laser. The solution we found in this aspect is very inefficient and if no commercial solution is available, it might be necessary

to develop one. With the development of fluoride glass fiber, strong absorption wavelength in the IR might become available in the future.

7.4 Outlook

We demonstrated the possibility of using OCT speckle intensity decorrelation for monitoring the thermal coagulation in real-time with a coregistered imaging and therapy system. The second-order correlation function was used to increase contrast of the coagulated tissue with noise correction to increase the possible monitoring depth and motion correction to increase the system robustness to motion. The developed system allowed for real-time monitoring of thermal coagulation.

A simulation of coagulation and motion induced decorrelation of intensity speckle pattern was realized to study the effects of motion on $g^{(2)}$ while in presence of coagulation. We were able to propose a correction method from it. Though the method remains approximative, it was essential to allow the continuous monitoring in the presence of motion. It also allowed us to discover the difference between the $g^{(2)}$ function induced by coagulation and motion. This opened the door to a new idea, possibly more motion robust, for monitoring the depth of coagulation. However, the new technique was not yet tested.

Our original approach still needs improvements, however, before being tested in the clinics. In-vivo testing needs to be done in order to confirm whether our approach is valid. An endoscopic probe also needs to be developed to allow testing in the esophagus for applications such as for the Barrett's esophagus.

We also explored the use of NN to replace $g^{(2)}$. Though some preliminary results were obtained, the method is, for now, not working on experimental data. The approach by AI is still a promising avenue as an alternative.

REFERENCES

[1] C. Boudoux, *Fundamentals of Biomedical Optics*. Blurb, Incorporated, Dec. 2016, google-Books-ID: AiBeMQAACAAJ.

[2] S. Zhang, "Finding the Right Color Palettes for Data Visualizations," Oct. 2018. [Online]. Available: https://blog.graphiq.com/finding-the-right-color-palettes-for-data-visualizations-fcd4e707a283

[3] P. Kovesi, "Good Colour Maps: How to Design Them," *arXiv:1509.03700 [cs]*, Sep. 2015, arXiv: 1509.03700. [Online]. Available: http://arxiv.org/abs/1509.03700

[4] S. L. Jacques, "Optical properties of biological tissues: a review," *Physics in Medicine and Biology*, vol. 58, no. 11, pp. R37–R61, May 2013. [Online]. Available: https://doi.org/10.1088%2F0031-9155%2F58%2F11%2Fr37

[5] S. Gabay, "Highlights of laser-tissue interaction mechanism," in *Laser Florence 2000: A Window on the Laser Medicine World*, vol. 4606. International Society for Optics and Photonics, Oct. 2001, pp. 30–33. [Online]. Available: https://www.spiedigitallibrary.org/conference-proceedings-of-spie/4606/0000/Highlights-of-laser-tissue-interaction-mechanism/10.1117/12.446714.short

[6] W. Sheng, S. He, W. J. Seare, and A. Almutairi, "Review of the progress toward achieving heat confinement—the holy grail of photothermal therapy," *Journal of Biomedical Optics*, vol. 22, no. 8, p. 080901, Aug. 2017. [Online]. Available: https://www.spiedigitallibrary.org/journals/Journal-of-Biomedical-Optics/volume-22/issue-8/080901/Review-of-the-progress-toward-achieving-heat-confinementthe-holy-grail/10.1117/1.JBO.22.8.080901.short

[7] J. T. Wei, P. Sharma, and N. J. Shaheen, "Endoscopic ablation therapies for Barrett's esophagus: a meta-analysis of stricture complications," *American Journal of Gastroenterology*, vol. 98, pp. NaN–NaN, 2003.

[8] N. J. Shaheen and D. J. Frantz, "When to consider endoscopic ablation therapy for Barrett's esophagus," *Current Opinion in Gastroenterology*, vol. 26, no. 4, pp. 361–366, Jul. 2010.

[9] S. Eluri and N. J. Shaheen, "Endoscopic Eradication Therapy in Barrett's Esophagus," *Techniques in Gastrointestinal Endoscopy*, vol. 19, no. 3, pp. 137–142, Jul. 2017.

[10] K. Kurokawa, S. Makita, Y.-J. Hong, and Y. Yasuno, "Two-dimensional micro-displacement measurement for laser coagulation using optical coherence tomography," *Biomedical Optics Express*, vol. 6, no. 1, pp. 170–190, Jan. 2015. [Online]. Available: https://www.osapublishing.org/boe/abstract.cfm?uri=boe-6-1-170

[11] W. Chang, Y. Fan, X. Zhang, and H. Liao, "An Intelligent Theranostics Method Using Optical Coherence Tomography Guided Automatic Laser Ablation for Neurosurgery," in *2018 40th Annual International Conference of the IEEE Engineering in Medicine and Biology Society (EMBC)*, Jul. 2018, pp. 3224–3227, iSSN: 1558-4615, 1557-170X.

[12] W. C. Y. Lo, N. Uribe-Patarroyo, A. S. Nam, M. Villiger, B. J. Vakoc, and B. E. Bouma, "Laser thermal therapy monitoring using complex differential variance in optical coherence tomography," *Journal of biophotonics*, vol. 10, no. 1, pp. 84–91, Jan. 2017. [Online]. Available: https://www.ncbi.nlm.nih.gov/pmc/articles/PMC5243231/

[13] W. C. Y. Lo, N. Uribe-Patarroyo, K. Hoebel, K. Beaudette, M. Villiger, N. S. Nishioka, B. J. Vakoc, and B. E. Bouma, "Balloon catheter-based radiofrequency ablation monitoring in porcine esophagus using optical coherence tomography," *Biomedical Optics Express*, vol. 10, no. 4, pp. 2067–2089, Apr. 2019. [Online]. Available: https://www.osapublishing.org/boe/abstract.cfm?uri=boe-10-4-2067

[14] S. Thomsen, "PATHOLOGIC ANALYSIS OF PHOTOTHERMAL AND PHOTOMECHANICAL EFFECTS OF LASER-TISSUE INTERACTIONS," *Photochemistry and Photobiology*, vol. 53, no. 6, pp. 825–835, Jun. 1991. [Online]. Available: http://doi.wiley.com/10.1111/j.1751-1097.1991.tb09897.x

[15] A. G. Doukas and T. J. Flotte, "Physical characteristics and biological effects of laser-induced stress waves," *Ultrasound in Medicine & Biology*, vol. 22, no. 2, pp. 151–164, Jan. 1996. [Online]. Available: http://www.sciencedirect.com/science/article/pii/0301562995020268

[16] M. Dyson, "Primary, secondary, and tertiary effects of phototherapy: a review," in *Mechanisms for Low-Light Therapy*, vol. 6140. International Society for Optics and Photonics, Feb. 2006, p. 614005. [Online]. Available: https://www.spiedigitallibrary.org/conference-proceedings-of-spie/6140/614005/Primary-secondary-and-tertiary-effects-of-phototherapy-a-review/10.1117/12.648449.short

[17] K. M. Kent and E. M. Graber, "Laser Tattoo Removal: A Review," *Dermatologic Surgery*, vol. 38, no. 1, pp. 1–13, 2012. [Online]. Available: https://onlinelibrary.wiley.com/doi/abs/10.1111/j.1524-4725.2011.02187.x

[18] H. Z. Alagha and M. Gülsoy, "Photothermal ablation of liver tissue with 1940-nm thulium fiber laser: an ex vivo study on lamb liver," *Journal of Biomedical Optics*, vol. 21, no. 1, p. 015007, Jan. 2016. [Online]. Available: http://biomedicaloptics.spiedigitallibrary.org/article.aspx?doi=10.1117/1.JBO.21.1.015007

[19] X. Fu, Z. Wang, H. Wang, Y. T. Wang, M. W. Jenkins, and A. M. Rollins, "Fiber-optic catheter-based polarization-sensitive OCT for radio-frequency ablation monitoring," *Optics letters*, vol. 39, no. 17, pp. 5066–5069, Sep. 2014. [Online]. Available: https://www.ncbi.nlm.nih.gov/pmc/articles/PMC4424424/

[20] O. Seror, M. Lepetit-Coiffé, B. Le Bail, B. D. de Senneville, H. Trillaud, C. Moonen, and B. Quesson, "Real time monitoring of radiofrequency ablation based on MR thermometry and thermal dose in the pig liver in vivo," *European Radiology*, vol. 18, no. 2, pp. 408–416, Feb. 2008. [Online]. Available: https://doi.org/10.1007/s00330-007-0761-4

[21] A. Bao, B. Goins, G. D. Dodd, A. Soundararajan, C. Santoyo, R. A. Otto, M. D. Davis, and W. T. Phillips, "Real-Time Iterative Monitoring of Radiofrequency Ablation Tumor Therapy with 15o-Water PET Imaging," *Journal of Nuclear Medicine*, vol. 49, no. 10, pp. 1723–1729, Oct. 2008. [Online]. Available: http://jnm.snmjournals.org/content/49/10/1723

[22] C. R. Munnerlyn, "Lasers in opthalmology: Past, present and future," *Journal of Modern Optics*, vol. 50, no. 15-17, pp. 2351–2360, Oct. 2003. [Online]. Available: https://doi.org/10.1080/09500340308233566

[23] F. Benboujja, S. Bowe, C. Boudoux, and C. Hartnick, "Utility of Optical Coherence Tomography for Guiding Laser Therapy Among Patients With Recurrent Respiratory Papillomatosis," *JAMA Otolaryngology– Head & Neck Surgery*, vol. 144, no. 9, pp. 831–837, Sep. 2018. [Online]. Available: https://www.ncbi.nlm.nih.gov/pmc/articles/PMC6233641/

[24] M.-L. Kuet and M. J. Pitman, "Photoangiolytic Laser Treatment of Recurrent Respiratory Papillomatosis: A Scaled Assessment," *Journal of Voice*, vol. 27, no. 1, pp. 124–128, Jan. 2013. [Online]. Available: http://www.sciencedirect.com/science/article/pii/S089219971200104X

[25] T. J. Pfefer, B. Choi, G. Vargas, K. M. McNally-Heintzelman, and A. J. Welch, "Mechanisms of laser-induced thermal coagulation of whole blood in vitro," R. R. Anderson, K. E. Bartels, L. S. Bass, D. J. Bornhop, C. G. Garrett, K. W. Gregory, N. Kollias, H. Lui, R. S. Malek, A. P. Perlmutter, H.-D. Reidenbach, L. Reinisch, D. S. Robinson, L. P. Tate, and E. A. Trowers, Eds., San Jose, CA, Jun. 1999, p. 20. [Online]. Available: http://proceedings.spiedigitallibrary.org/proceeding.aspx?doi=10.1117/12.350970

[26] K. Beaudette, "Double-Clad Fiber-Based Systems and Devices as a Therapeutic and Diagnostic Tool for Barrett's Esophagus," phd, École Polytechnique de Montréal, Jun. 2017. [Online]. Available: https://publications.polymtl.ca/2602/

[27] M. Villiger, "Injury depth control from combined wavelength and power tuning in scanned beam laser thermal therapy," *Journal of Biomedical Optics*, vol. 16, no. 11, p. 118001, Nov. 2011. [Online]. Available: http://biomedicaloptics.spiedigitallibrary.org/article.aspx?doi=10.1117/1.3647581

[28] W. Cheong, S. Prahl, and A. Welch, "A review of the optical properties of biological tissues," *IEEE Journal of Quantum Electronics*, vol. 26, no. 12, pp. 2166–2185, Dec. 1990. [Online]. Available: http://ieeexplore.ieee.org/document/64354/

[29] J. Crank, *The mathematics of diffusion*, 2nd ed. Oxford, [Eng]: Clarendon Press, 1975.

[30] B. M. Mirdan, "Laser induced clot formation in blood treated by EDTA," *Natural Science*, vol. 5, no. 7, pp. 796–799, Jul. 2013. [Online]. Available: http://www.scirp.org/Journal/Paperabs.aspx?paperid=34111

[31] L. Polese, I. Angriman, M. Scarpa, D. Pagano, P. Parente, F. Erroi, M. Frego, D. F. D'Amico, and L. Norberto, "Diode laser treatment of Barrett's esophagus: long-term results," *Lasers in Medical Science*, vol. 26, no. 2, pp. 223–228, Mar. 2011. [Online]. Available: https://doi.org/10.1007/s10103-010-0836-3

[32] K. K. Wang and J. Y. Kim, "Photodynamic therapy in Barrett's esophagus," *Gastrointestinal Endoscopy Clinics of North America*, vol. 13, no. 3, pp. 483–489, Jul. 2003. [Online]. Available: https://linkinghub.elsevier.com/retrieve/pii/S1052515703000497

[33] L. Gossner, A. May, M. Stolte, G. Seitz, E. G. Hahn, and C. Ell, "KTP laser destruction of dysplasia and early cancer in columnar-lined Barrett's esophagus," *Gastrointestinal Endoscopy*, vol. 49, no. 1, pp. 8–12, Jan. 1999.

[34] A. Sibille, R. Lambert, J.-C. Souquet, G. Sabben, and F. Descos, "Long-term survival after photodynamic therapy for esophageal cancer," *Gastroenterology*, vol. 108, no. 2, pp. 337–344, Feb. 1995. [Online]. Available: http://www.sciencedirect.com/science/article/pii/0016508595900586

[35] K. Beaudette, H. W. Baac, W.-J. Madore, M. Villiger, N. Godbout, B. E. Bouma, and C. Boudoux, "Laser tissue coagulation and concurrent optical coherence tomography through a double-clad fiber coupler," *Biomedical Optics Express*, vol. 6, no. 4, p. 1293, Apr. 2015. [Online]. Available: https://www.osapublishing.org/abstract.cfm?URI=boe-6-4-1293

[36] W. Drexler and J. G. Fujimoto, Eds., *Optical coherence tomography: technology and applications*, 2nd ed. Cham: Springer, 2015, oCLC: 919429452.

[37] X. Attendu, R. M. Ruis, C. Boudoux, T. G. v. Leeuwen, and D. J. Faber, "Simple and robust calibration procedure for k-linearization and dispersion compensation in optical coherence tomography," *Journal of Biomedical Optics*, vol. 24, no. 5, p. 056001, May 2019. [Online]. Available: https://www.spiedigitallibrary.org/journals/Journal-of-Biomedical-Optics/volume-24/issue-5/056001/----Custom-HTML----Simple/10.1117/1.JBO.24.5.056001.short

[38] M. Wojtkowski, V. J. Srinivasan, T. H. Ko, J. G. Fujimoto, A. Kowalczyk, and J. S. Duker, "Ultrahigh-resolution, high-speed, Fourier domain optical coherence tomography and methods for dispersion compensation," *Optics Express*, vol. 12, no. 11, pp. 2404–2422, May 2004. [Online]. Available: https://www.osapublishing.org/oe/abstract.cfm?uri=oe-12-11-2404

[39] B. Baumann, C. W. Merkle, R. A. Leitgeb, M. Augustin, A. Wartak, M. Pircher, and C. K. Hitzenberger, "Signal averaging improves signal-to-noise in OCT images: But which approach works best, and when?" *Biomedical Optics Express*, vol. 10, no. 11, p. 5755, Nov. 2019. [Online]. Available: https://www.osapublishing.org/abstract.cfm?URI=boe-10-11-5755

[40] J. Goodman, *Speckle Phenomena in Optics: Theory and Applications*. Roberts & Company, 2007. [Online]. Available: https://books.google.ca/books?id=TynXEcS0DncC

[41] V. Y. Zaitsev, L. A. Matveev, A. L. Matveyev, G. V. Gelikonov, and V. M. Gelikonov, "A model for simulating speckle-pattern evolution based on close to reality procedures used in spectral-domain OCT," *arXiv:1406.3448 [physics]*, Jun. 2014, arXiv: 1406.3448. [Online]. Available: http://arxiv.org/abs/1406.3448

[42] A. S. Nam, I. Chico-Calero, and B. J. Vakoc, "Complex differential variance algorithm for optical coherence tomography angiography," *Biomedical Optics Express*, vol. 5, no. 11, p. 3822, Nov. 2014. [Online]. Available: https://www.osapublishing.org/boe/abstract.cfm?uri=boe-5-11-3822

[43] B. Braaf, S. Donner, A. S. Nam, B. E. Bouma, and B. J. Vakoc, "Complex differential variance angiography with noise-bias correction for optical coherence tomography of the retina," *Biomedical Optics Express*, vol. 9, no. 2, p. 486, Feb. 2018. [Online]. Available: https://www.osapublishing.org/abstract.cfm?URI=boe-9-2-486

[44] Z. Li, H. Li, Y. He, S. Cai, and S. Xie, "A model of speckle contrast in optical coherence tomography for characterizing the scattering coefficient of homogenous tissues," *Physics in Medicine and Biology*, vol. 53, no. 20, pp. 5859–5866, Oct. 2008. [Online]. Available: http://stacks.iop.org/0031-9155/53/i=20/a=020?key=crossref.c27bf442c58fab12f959a433b5ea04c0

[45] N. Yokoi, Y. Aizu, and J. Uozumi, "Analysis of blood coagulation process based on fractality and dynamic characteristic of laser speckle pattern," *Journal of Biomedical Optics*, vol. 24, no. 03, p. 1, Dec. 2018. [Online]. Available: https://www.spiedigitallibrary.org/journals/journal-of-biomedical-optics/volume-24/issue-03/031018/Analysis-of-blood-coagulation-process-based-on-fractality-and-dynamic/10.1117/1.JBO.24.3.031018.full

[46] X. Liu, Y. Huang, and J. U. Kang, "Distortion-free freehand-scanning OCT implemented with real-time scanning speed variance correction," *Optics Express*, vol. 20, no. 15, pp. 16 567–16 583, Jul. 2012. [Online]. Available: https://www.osapublishing.org/oe/abstract.cfm?uri=oe-20-15-16567

[47] N. Uribe-Patarroyo and B. E. Bouma, "Rotational distortion correction in endoscopic optical coherence tomography based on speckle decorrelation," *Optics Letters*, vol. 40, no. 23, p. 5518, Dec. 2015. [Online]. Available: https://www.osapublishing.org/abstract.cfm?URI=ol-40-23-5518

[48] C. Lee, G. Cheon, D.-H. Kim, and J. U. Kang, "Feasibility study: protein denaturation and coagulation monitoring with speckle variance optical coherence tomography," *Journal of Biomedical Optics*, vol. 21, no. 12, p. 125004, Dec. 2016. [Online]. Available: http://biomedicaloptics.spiedigitallibrary.org/article.aspx?doi=10.1117/1.JBO.21.12.125004

[49] K. Beaudette, M. Strupler, J. Ren, B. E. Bouma, and C. Boudoux, "Radiometric model for coaxial single- and multimode optical emission from double-clad fiber," *Applied Optics*, vol. 57, no. 5, p. 1110, Feb. 2018. [Online]. Available: https://www.osapublishing.org/abstract.cfm?URI=ao-57-5-1110

[50] W.-J. Madore, E. D. Montigny, O. Ouellette, S. Lemire-Renaud, M. Leduc, X. Daxhelet, N. Godbout, and C. Boudoux, "Asymmetric double-clad fiber couplers for endoscopy," *Optics Letters*, vol. 38, no. 21, pp. 4514–4517, Nov. 2013. [Online]. Available: https://www.osapublishing.org/ol/abstract.cfm?uri=ol-38-21-4514

[51] S. Lemire-Renaud, M. Strupler, F. Benboujja, N. Godbout, and C. Boudoux, "Double-clad fiber with a tapered end for confocal endomicroscopy," *Biomedical Optics Express*, vol. 2, no. 11, pp. 2961–2972, Nov. 2011. [Online]. Available: https://www.osapublishing.org/boe/abstract.cfm?uri=boe-2-11-2961

[52] S. Lemire-Renaud, M. Rivard, M. Strupler, D. Morneau, F. Verpillat, X. Daxhelet, N. Godbout, and C. Boudoux, "Double-clad fiber coupler for endoscopy," *Optics Express*, vol. 18, no. 10, pp. 9755–9764, May 2010. [Online]. Available: https://www.osapublishing.org/oe/abstract.cfm?uri=oe-18-10-9755

[53] S. Toupin, P. Bour, M. Lepetit-Coiffé, V. Ozenne, B. Denis de Senneville, R. Schneider, A. Vaussy, A. Chaumeil, H. Cochet, F. Sacher, P. Jaïs, and B. Quesson, "Feasibility of real-time MR thermal dose mapping for predicting radiofrequency ablation outcome in the myocardium in vivo," *Journal of Cardiovascular Magnetic Resonance*, vol. 19, Jan. 2017. [Online]. Available: https://www.ncbi.nlm.nih.gov/pmc/articles/PMC5286737/

[54] H. Ke, S. Tai, and L. V. Wang, "Photoacoustic thermography of tissue," *Journal of Biomedical Optics*, vol. 19, no. 2, Feb. 2014. [Online]. Available: https://www.ncbi.nlm.nih.gov/pmc/articles/PMC3922142/

[55] J. Shah, S. Park, S. Aglyamov, T. Larson, L. Ma, K. Sokolov, K. Johnston, T. Milner, and S. Y. Emelianov, "Photoacoustic imaging and temperature measurement for photothermal cancer therapy," *Journal of biomedical optics*, vol. 13, no. 3, p. 034024, 2008. [Online]. Available: https://www.ncbi.nlm.nih.gov/pmc/articles/PMC2713867/

[56] A. H. Kashani, C.-L. Chen, J. K. Gahm, F. Zheng, G. M. Richter, P. J. Rosenfeld, Y. Shi, and R. K. Wang, "Optical Coherence Tomography Angiography: A Comprehensive Review of Current Methods and Clinical Applications," *Progress in retinal and eye research*, vol. 60, pp. 66–100, Sep. 2017. [Online]. Available: https://www.ncbi.nlm.nih.gov/pmc/articles/PMC5600872/

[57] J. F. d. Boer, S. M. Srinivas, A. Malekafzali, Z. Chen, and J. S. Nelson, "Imaging thermally damaged tissue by polarization sensitive optical coherence tomography," *Optics Express*, vol. 3, no. 6, pp. 212–218, Sep. 1998. [Online]. Available: https://www.osapublishing.org/oe/abstract.cfm?uri=oe-3-6-212

[58] K. Schoenenberger, B. W. Colston, D. J. Maitland, L. B. D. Silva, and M. J. Everett, "Mapping of birefringence and thermal damage in tissue by use of polarization-sensitive optical coherence tomography," *Applied Optics*, vol. 37, no. 25, pp. 6026–6036, Sep. 1998. [Online]. Available: https://www.osapublishing.org/ao/abstract.cfm?uri=ao-37-25-6026

[59] I. Ahmad, A. Gribble, I. Murtza, M. Ikram, M. Pop, and A. Vitkin, "Polarization image segmentation of radiofrequency ablated porcine myocardial tissue," *PLoS ONE*, vol. 12, no. 4, Apr. 2017. [Online]. Available: https://www.ncbi.nlm.nih.gov/pmc/articles/PMC5381909/

[60] K. Kurokawa, S. Makita, and Y. Yasuno, "Investigation of Thermal Effects of Photocoagulation on Retinal Tissue Using Fine-Motion-Sensitive Dynamic Optical Coherence Tomography," *PLOS ONE*, vol. 11, no. 6, p. e0156761, Jun. 2016. [Online]. Available: https://journals.plos.org/plosone/article?id=10.1371/journal.pone.0156761

[61] K. Kurokawa, S. Makita, Y.-J. Hong, and Y. Yasuno, "In-plane and out-of-plane tissue micro-displacement measurement by correlation coefficients of optical coherence tomography," *Optics Letters*, vol. 40, no. 9, pp. 2153–2156, May 2015. [Online]. Available: https://www.osapublishing.org/ol/abstract.cfm?uri=ol-40-9-2153

[62] H. H. Müller, L. Ptaszynski, K. Schlott, C. Debbeler, M. Bever, S. Koinzer, R. Birngruber, R. Brinkmann, and G. Hüttmann, "Imaging thermal expansion and retinal tissue changes during photocoagulation by high speed OCT," *Biomedical Optics Express*, vol. 3, no. 5, pp. 1025–1046, Apr. 2012. [Online]. Available: https://www.ncbi.nlm.nih.gov/pmc/articles/PMC3342180/

[63] B. J. Vakoc, G. J. T. M.d, and B. E. Bouma, "Real-time microscopic visualization of tissue response to laser thermal therapy," *Journal of Biomedical Optics*, vol. 12, no. 2, p. 020501, Mar. 2007. [Online]. Available: https://www.spiedigitallibrary.org/journals/Journal-of-Biomedical-Optics/volume-12/issue-2/020501/Real-time-microscopic-visualization-of-tissue-response-to-laser-thermal/10.1117/1.2714027.short

[64] N. Uribe-Patarroyo, M. Villiger, and B. E. Bouma, "Quantitative technique for robust and noise-tolerant speed measurements based on speckle decorrelation in optical coherence tomography," *Optics Express*, vol. 22, no. 20, p. 24411, Oct. 2014. [Online]. Available: https://www.osapublishing.org/oe/abstract.cfm?uri=oe-22-20-24411

[65] "Early Photocoagulation for Diabetic Retinopathy," *Ophthalmology*, vol. 98, no. 5, pp. 766–785, May 1991. [Online]. Available: https://linkinghub.elsevier.com/retrieve/pii/S0161642013380117

[66] "Photocoagulation for Diabetic Macular Edema: Early Treatment Diabetic Retinopathy Study Report Number 1 Early Treatment Diabetic Retinopathy Study Research Group," *Archives of Ophthalmology*, vol. 103, no. 12, p. 1796, Dec. 1985. [Online]. Available: http://archopht.jamanetwork.com/article.aspx?doi=10.1001/archopht.1985.01050120030015

[67] S. Sivaprasad and G. Dorin, "Subthreshold diode laser micropulse photocoagulation for the treatment of diabetic macular edema," *Expert Review of Medical Devices*, vol. 9, no. 2, pp. 189–197, Mar. 2012. [Online]. Available: https://doi.org/10.1586/erd.12.1

[68] S. S. Hayreh, P. A. Podhajsky, and M. B. Zimmerman, "Natural History of Visual Outcome in Central Retinal Vein Occlusion," *Ophthalmology*, vol. 118, no. 1, pp. 119–133.e2, Jan. 2011. [Online]. Available: https://www.ncbi.nlm.nih.gov/pmc/articles/PMC2989417/

[69] "Argon Laser Scatter Photocoagulation for Prevention of Neovascularization and Vitreous Hemorrhage in Branch Vein Occlusion: A Randomized Clinical Trial," *Archives of Ophthalmology*, vol. 104, no. 1, p. 34, Jan. 1986. [Online]. Available: http://archopht.jamanetwork.com/article.aspx?doi=10.1001/archopht.1986.01050130044017

[70] J. Shah, S. R. Aglyamov, K. Sokolov, T. E. Milner, and S. Y. Emelianov, "Ultrasound imaging to monitor photothermal therapy – Feasibility study," *Optics Express*, vol. 16, no. 6, pp. 3776–3785, Mar. 2008. [Online]. Available: https://www.osapublishing.org/oe/abstract.cfm?uri=oe-16-6-3776

[71] P. Saccomandi, E. Schena, and S. Silvestri, "Techniques for temperature monitoring during laser-induced thermotherapy: An overview," *International Journal of Hyperthermia*, vol. 29, no. 7, pp. 609–619, Nov. 2013. [Online]. Available: https://www.tandfonline.com/doi/citedby/10.3109/02656736.2013.832411

[72] R. Medvid, A. Ruiz, R. J. Komotar, J. R. Jagid, M. E. Ivan, R. M. Quencer, and M. B. Desai, "Current Applications of MRI-Guided Laser Interstitial Thermal Therapy in the Treatment of Brain Neoplasms and Epilepsy: A Radiologic and Neurosurgical Overview," *American Journal of Neuroradiology*, vol. 36, no. 11, pp. 1998–2006, Nov. 2015. [Online]. Available: http://www.ajnr.org/content/36/11/1998

[73] Z. Tovar-Spinoza, D. Carter, D. Ferrone, Y. Eksioglu, and S. Huckins, "The use of MRI-guided laser-induced thermal ablation for epilepsy," *Child's Nervous System: ChNS: Official Journal of the International Society for Pediatric Neurosurgery*, vol. 29, no. 11, pp. 2089–2094, Nov. 2013.

[74] B. J. Vakoc, M. Shishko, S. H. Yun, W.-Y. Oh, M. J. Suter, A. E. Desjardins, J. A. Evans, N. S. Nishioka, G. J. Tearney, and B. E. Bouma, "Comprehensive esophageal microscopy by using optical frequency-domain imaging (with video)," *Gastrointestinal endoscopy*, vol. 65, no. 6, pp. 898–905, May 2007. [Online]. Available: https://www.ncbi.nlm.nih.gov/pmc/articles/PMC2705339/

[75] M. J. Suter, M. J. Gora, G. Y. Lauwers, T. Arnason, J. Sauk, K. A. Gallagher, L. Kava, K. M. Tan, A. R. Soomro, T. P. Gallagher, J. A. Gardecki, B. E. Bouma, M. Rosenberg, N. S. Nishioka, and G. J. Tearney, "Esophageal-guided biopsy with volumetric laser endomicroscopy and laser cautery marking: a pilot clinical study," *Gastrointestinal Endoscopy*, vol. 79, no. 6, pp. 886–896, Jun. 2014.

[76] M. J. Suter, B. J. Vakoc, P. S. Yachimski, M. Shishkov, G. Y. Lauwers, M. Mino-Kenudson, B. E. Bouma, N. S. Nishioka, and G. J. Tearney, "Comprehensive microscopy of the esophagus in human patients with optical frequency domain imaging," *Gastrointestinal Endoscopy*, vol. 68, no. 4, pp. 745–753, Oct. 2008.

[77] T. J. Pfefer, B. Choi, G. Vargas, K. M. McNally-Heintzelman, and A. J. Welch, "Mechanisms of laser-induced thermal coagulation of whole blood in vitro," in *Lasers in Surgery: Advanced Characterization, Therapeutics, and Systems IX*, vol. 3590. International Society for Optics and Photonics, Jun. 1999, pp. 20–31. [Online]. Available: https://www.spiedigitallibrary.org/conference-proceedings-of-spie/3590/0000/Mechanisms-of-laser-induced-thermal-coagulation-of-whole-blood-in/10.1117/12.350970.short

[78] Y. Bromberg, Y. Lahini, E. Small, and Y. Silberberg, "Hanbury Brown and Twiss interferometry with interacting photons," *Nature Photonics*, vol. 4, no. 10, pp. 721–726, Oct. 2010. [Online]. Available: https://www.nature.com/articles/nphoton.2010.195

[79] N. Uribe-Patarroyo, A. L. Post, S. Ruiz-Lopera, D. J. Faber, and B. E. Bouma, "Noise and bias in optical coherence tomography signal decorrelation," *Submitted to OSA Continuum*.

[80] S. Makita, K. Kurokawa, Y.-J. Hong, M. Miura, and Y. Yasuno, "Noise-immune complex correlation for optical coherence angiography based on standard and Jones matrix optical coherence tomography," *Biomedical Optics Express*, vol. 7, no. 4, pp. 1525–1548, Mar. 2016. [Online]. Available: https://www.ncbi.nlm.nih.gov/pmc/articles/PMC4929659/

[81] R. Shao and L. Chang, "A new maximum power point tracking method for photovoltaic arrays using golden section search algorithm," in *2008 Canadian Conference on Electrical and Computer Engineering*, May 2008, pp. 000 619–000 622, iSSN: 0840-7789.

[82] J. H. Fugett, H. Bennett, J. Shrout, and J. Coad, "Nitro Blue Tetrazolium (NBT) Staining as an Assessment of Thermal Penetration," *The FASEB Journal*, vol. 31, no. 1_supplement, pp. 984.3–984.3, Apr. 2017. [Online]. Available: https://www.fasebj.org/doi/abs/10.1096/fasebj.31.1_supplement.984.3

[83] L. M. Oliveira, A. L. V. S. Lage, M. P. P. Clemente, and V. V. Tuchin, "Rat muscle opacity decrease due to the osmosis of a simple mixture," *Journal of Biomedical Optics*, vol. 15, no. 5, p. 055004, Sep. 2010. [Online]. Available: https://www.spiedigitallibrary.org/journals/Journal-of-Biomedical-Optics/volume-15/issue-5/055004/Rat-muscle-opacity-decrease-due-to-the-osmosis-of-a/10.1117/1.3486539.short

[84] L. Oliveira, A. Lage, M. Pais Clemente, and V. Tuchin, "Optical characterization and composition of abdominal wall muscle from rat," *Optics and Lasers in Engineering*, vol. 47, no. 6, pp. 667–672, Jun. 2009. [Online]. Available: http://www.sciencedirect.com/science/article/pii/S014381660800256X

[85] A. J. Welch and M. J. v. Gemert, Eds., *Optical-Thermal Response of Laser-Irradiated Tissue*, 2nd ed. Springer Netherlands, 2011.

[86] J. Lee, W. Wu, J. Y. Jiang, B. Zhu, and D. A. Boas, "Dynamic light scattering optical coherence tomography," *Optics Express*, vol. 20, no. 20, pp. 22 262–22 277, Sep. 2012. [Online]. Available: https://www.osapublishing.org/oe/abstract.cfm?uri=oe-20-20-22262

[87] N. Weiss, T. G. v. Leeuwen, and J. Kalkman, "Localized measurement of longitudinal and transverse flow velocities in colloidal suspensions using optical coherence tomography." *Physical review. E, Statistical, nonlinear, and soft matter physics*, vol. 88, no. 4, p. 042312, 2013.

[88] N. Uribe-Patarroyo and B. E. Bouma, "Velocity gradients in spatially-resolved laser Doppler flowmetry and dynamic light scattering with confocal and coherence gating," *Physical review. E*, vol. 94, no. 2-1, p. 022604, Aug. 2016. [Online]. Available: https://www.ncbi.nlm.nih.gov/pmc/articles/PMC5059111/

[89] R. Maltais-Tariant, "Real-time OCT surveillance of laser therapy through speckle decorrelation," Master's thesis, École Polytechnique de Montréal, 2019.

[90] M. Guizar-Sicairos, S. T. Thurman, and J. R. Fienup, "Efficient subpixel image registration algorithms," *Optics Letters*, vol. 33, no. 2, p. 156, Jan. 2008. [Online]. Available: https://www.osapublishing.org/abstract.cfm?URI=ol-33-2-156

[91] H. S. Stone, M. T. Orchard, E.-C. Chang, and S. A. Martucci, "A fast direct Fourier-based algorithm for subpixel registration of images," *IEEE Trans. Geoscience and Remote Sensing*, vol. 39, pp. 2235–2243, 2001.

[92] B. Reddy and B. Chatterji, "An FFT-based technique for translation, rotation, and scale-invariant image registration," *IEEE Transactions on Image Processing*, vol. 5, no. 8, pp. 1266–1271, Aug. 1996. [Online]. Available: http://ieeexplore.ieee.org/document/506761/

[93] M. L. Gabriele, G. Wollstein, H. Ishikawa, J. Xu, J. Kim, L. Kagemann, L. S. Folio, and J. S. Schuman, "Three Dimensional Optical Coherence Tomography Imaging: Advantages and Advances," *Progress in retinal and eye research*, vol. 29, no. 6, pp. 556–579, Nov. 2010. [Online]. Available: https://www.ncbi.nlm.nih.gov/pmc/articles/PMC2962728/

[94] B. Braaf, K. V. Vienola, C. K. Sheehy, Q. Yang, K. A. Vermeer, P. Tiruveedhula, D. W. Arathorn, A. Roorda, and J. F. de Boer, "Real-time eye motion correction in phase-resolved OCT angiography with tracking SLO," *Biomedical Optics Express*, vol. 4, no. 1, pp. 51–65, Dec. 2012. [Online]. Available: https://www.ncbi.nlm.nih.gov/pmc/articles/PMC3539196/

[95] Y. Watanabe, Y. Takahashi, and H. Numazawa, "Graphics processing unit accelerated intensity-based optical coherence tomography angiography using differential frames

with real-time motion correction," *Journal of Biomedical Optics*, vol. 19, no. 2, p. 021105, Jul. 2013. [Online]. Available: http://biomedicaloptics.spiedigitallibrary.org/article.aspx?doi=10.1117/1.JBO.19.2.021105

[96] G. Liu, W. Qi, L. Yu, and Z. Chen, "Real-time bulk-motion-correction free Doppler variance optical coherence tomography for choroidal capillary vasculature imaging," *Optics Express*, vol. 19, no. 4, p. 3657, Feb. 2011. [Online]. Available: https://www.osapublishing.org/oe/abstract.cfm?uri=oe-19-4-3657

[97] M. F. Kraus, B. Potsaid, M. A. Mayer, R. Bock, B. Baumann, J. J. Liu, J. Hornegger, and J. G. Fujimoto, "Motion correction in optical coherence tomography volumes on a per A-scan basis using orthogonal scan patterns," *Biomedical Optics Express*, vol. 3, no. 6, pp. 1182–1199, May 2012. [Online]. Available: https://www.ncbi.nlm.nih.gov/pmc/articles/PMC3370961/

[98] A. Ahmad, S. G. Adie, E. J. Chaney, U. Sharma, and S. A. Boppart, "Cross-correlation-based image acquisition technique for manually-scanned optical coherence tomography," *Optics Express*, vol. 17, no. 10, p. 8125, May 2009. [Online]. Available: https://www.osapublishing.org/oe/abstract.cfm?uri=oe-17-10-8125

[99] D. Stathakis, "How many hidden layers and nodes?" *International Journal of Remote Sensing*, vol. 30, no. 8, pp. 2133–2147, Apr. 2009. [Online]. Available: https://www.tandfonline.com/doi/full/10.1080/01431160802549278

[100] J. Heaton, *Artificial Intelligence for Humans, Volume 3: Deep Learning and Neural Networks*. CreateSpace Independent Publishing Platform, 2015. [Online]. Available: https://books.google.ca/books?id=q9mijgEACAAJ

[101] J. Brownlee, "How to Configure the Number of Layers and Nodes in a Neural Network," Jul. 2018. [Online]. Available: https://machinelearningmastery.com/how-to-configure-the-number-of-layers-and-nodes-in-a-neural-network/